




Wave- and Tide-Induced Infragravity Dynamics at an Intermediate-To-Dissipative Microtidal Beach

 Lorenzo Melito¹ , Luca Parlagreco² , Saverio Devoti², and Maurizio Brocchini¹ 
¹Department of Civil Engineering and Architecture (DICEA), Università Politecnica delle Marche, Ancona, Italy, ²Italian Institute for Environmental Protection and Research (ISPRA), Rome, Italy

Key Points:

- Storms and tide are simulated with XBeach through an innovative calibration approach, to study infragravity waves at Sabaudia (Italy)
- Bound long waves grow in the shoaling zone and stop growing/decay in the surf zone, with no shoreline dissipation
- Albeit small, tidal excursion significantly alters onshore fluxes and reflection coefficients for intermediate IG frequencies

Correspondence to:

 L. Melito,
l.melito@univpm.it

Citation:

 Melito, L., Parlagreco, L., Devoti, S., & Brocchini, M. (2022). Wave- and tide-induced infragravity dynamics at an intermediate-to-dissipative microtidal beach. *Journal of Geophysical Research: Oceans*, 127, e2021JC017980. <https://doi.org/10.1029/2021JC017980>

 Received 6 SEP 2021
Accepted 8 APR 2022

Author Contributions:

Conceptualization: Lorenzo Melito, Luca Parlagreco, Saverio Devoti, Maurizio Brocchini
Data curation: Lorenzo Melito, Luca Parlagreco, Saverio Devoti
Formal analysis: Lorenzo Melito
Funding acquisition: Luca Parlagreco, Saverio Devoti, Maurizio Brocchini
Investigation: Lorenzo Melito, Maurizio Brocchini
Methodology: Lorenzo Melito, Maurizio Brocchini
Project Administration: Luca Parlagreco, Saverio Devoti, Maurizio Brocchini
Resources: Luca Parlagreco, Saverio Devoti
Software: Lorenzo Melito, Luca Parlagreco, Saverio Devoti

© 2022 The Authors.

 This is an open access article under the terms of the [Creative Commons Attribution-NonCommercial License](https://creativecommons.org/licenses/by/4.0/), which permits use, distribution and reproduction in any medium, provided the original work is properly cited and is not used for commercial purposes.

Abstract Numerical simulations of a range of wave climates and tide conditions made with the model XBeach are exploited to study propagation, evolution, dissipation, and reflection patterns of infragravity waves (IGW) at the intermediate-to-dissipative beach of Sabaudia (Tyrrhenian sea, Italy). On the basis of a novel calibration process performed using field swash properties collected by a nearby monitoring station, the model reproduces average run-up characteristics with good skill (Willmott index of agreement of 0.61 for $R_{2\%}$). IGW at Sabaudia beach evolves exclusively as bound long waves growing across the shoaling region for both mild and intense wave climates. Furthermore, values of the dimensionless bed slope β_H at which transition from steep-to mild-slope behavior occurs are higher than the threshold commonly assumed in the literature. Finally, although the small tide (0.4 m between mean high water spring and mean high water spring; tide range/breaking wave amplitude ratios between 0.14 and 1.1) does not alter bulk IGW reflection significantly, low tide is effective in reducing onshore IGW fluxes and, ultimately, reflection coefficients R^2 selectively for intermediate IG frequencies. Our study, for the first time, gives clear evidence that the tide has a role in determining frequency-dependent IGW dynamics and altering the dissipative state of a mild sloping beach also in a microtidal environment.

Plain Language Summary Infragravity waves (IGW) are long-period oscillations of the water level, usually underlying common short waves. They are relevant to a number of coastal processes, like beach inundation and sand mobilization. A set of storm conditions and tidal levels is here simulated with a computer to observe how IGW evolves and dissipates at the beach of Sabaudia (Italy), characterized by low slopes and a small tidal excursion. It is found that IGW at Sabaudia develop and intensifies by gaining energy from short wind waves as they travel toward the shore. IGW are eventually set free to propagate where short waves start to break, and then stop growing or begin to decay due to the increasing dissipation they meet when they travel in low waters. The presence of IGW at Sabaudia is dominant, especially during intense storms. We have also seen that the variation of the tidal level at Sabaudia is capable of changing how much of the IGW energy is able to reach the shore, mainly for an intermediate range of IGW wave periods. We suggest that tide should be taken into account when evaluating beach inundation due to waves, even on coasts when the tidal range is small.

1. Introduction

Infragravity waves (IGW hereafter) are low-frequency oscillations of the water surface with periods of 20–30 s to 5 min or more, mostly generated as either long-period oscillations forced by short wave groups (bound long waves, BLW; Longuet-Higgins & Stewart [1964]) or free waves triggered by cross-shore variation of the breakpoint due to differential breaking of waves within individual wave groups (breakpoint-forced long waves, BFLW; Symonds et al. [1982]). Field and experimental investigations have ascertained the influence of IGW on a number of nearshore processes, such as sediment transport and subsequent morphological evolution of sandy beaches (Baldock et al., 2010; de Bakker et al., 2016), tidal inlet dynamics (Bertin & Olabarrieta, 2016; Williams & Stacey, 2016), swash and run-up characteristics (Ruessink et al., 1998; Ruggiero et al., 2001), dune erosion (Roelvink et al., 2009), and seiche (Okiihiro et al., 1993). A thorough review of the features and dynamics of IGW is given in Bertin et al. (2018).

It is now acknowledged that IGW-related processes are frequency-dependent. Battjes et al. (2004) analyzed experimental data of waves propagating over a barred profile and concluded that the growth rate of IGW increases with increasing frequency, implying a dependence on the energy transfer from short to long (bound) waves. Field data

Supervision: Luca Parlagreco, Saverio Devoti, Maurizio Brocchini
Validation: Lorenzo Melito
Visualization: Lorenzo Melito
Writing – original draft: Lorenzo Melito
Writing – review & editing: Lorenzo Melito, Luca Parlagreco, Saverio Devoti, Maurizio Brocchini

examined by de Bakker et al. (2014) revealed a strong dissipation of high-frequency IGW, whereas low-frequency IGW shows a standing wave pattern, with increased IG reflection at the shoreline and minimal dissipation.

Also, tide is shown to exert an influence over the amount of dissipation and reflection of infragravity energy on a coast. Tidal modulation of IGW reflection has been observed by, for example, Okihiro and Guza (1995) and Bertin et al. (2020) with a larger reflection of IG energy at the shore during high tide than during low tide. This occurs because the sea level rise due to high tide allows waves to meet the shore at the upper portion of the intertidal beach, which is generally steeper than its lower part, especially on coasts with a considerable tidal range. A larger loss of IG energy over a (convex) low-tide surf zone than over a (concave) high-tide surf zone has also been discussed by Thomson et al. (2006).

Most of the aforementioned conclusions on low-frequency waves evolution on the nearshore have been achieved mainly for meso- and macrotidal oceanic coasts, whereas the corresponding IG mechanisms emerging at microtidal beaches have been comparatively less studied. In this study, we present an analysis of infragravity-related dynamics at the mildly sloping, microtidal beach of Sabaudia (central Tyrrhenian sea, Italy). The relevant generation, dissipation, and reflection mechanisms of IGW are analyzed by means of the numerical model XBeach (Roelvink et al., 2009; Ruffini et al., 2020). The model is first calibrated using a novel approach that combines field observations of run-up collected by a nearby video-monitoring station, and hindcast data from the freely available oceanographic model of the European Union Copernicus Marine Service. The novel approach is rather straightforward to apply and exploits only standard video products, making it appealing to use when hydrological field data are not available. The calibrated XBeach is then tested against a set of statistically significant synthetic storms covering a range of offshore wave heights, allowing for the study of IGW features across mild to extreme wave conditions. Our work contributes to improving our understanding of low-frequency wave dynamics at microtidal coasts typical of the Mediterranean basin. A description of the study site, wave climate features, video-monitoring facility, and modeling set-up is given in Section 2. Results of the calibration process and IG analysis are given in Section 3 and discussed in Section 4. Concluding remarks are given in Section 5.

2. Materials and Methods

2.1. Study Site

The investigated beach lies within the municipality of Sabaudia (Lazio region, central Italy) and is part of the Circeo National Park, one of the oldest natural reserves in Italy. Located along the middle Tyrrhenian Sea, the Sabaudia coastline presents a NW–SE orientation and faces approximately 250° from the north (Figure 1a). The tidal regime in the area is microtidal and semi-diurnal with the tidal range rarely exceeding 0.5 m, and tide-related currents may be taken as negligible. Native sediment consists of medium-to-fine sand with $d_{50} = 0.14$ mm at around 10 m depth, and $d_{50} = 0.3$ mm at the beach face (Parlagreco et al., 2019).

The submerged beach usually presents two or three bars (Parlagreco et al., 2019). The outer bar is mostly linear whereas the inner bars show some sinuosity, typical of a Rhythmic Bar and Beach (RBB) morphology. The inner bars are occasionally interrupted by rip channels common for a Transverse Bar and Rip (TBR) state (Taramelli et al., 2020).

2.2. Wave Climate and Beach State

The lack of nearby wave buoys hinders the collection of in situ wave climate observations. To make up for this deficiency, wave data for the following analyses are obtained from the hindcast Mediterranean Sea Waves oceanographic model run by the EU Copernicus Marine Service CMEMS (Korres et al., 2019).

Hourly values of modeled significant wave heights H_s , mean (zero-crossing) wave periods T_0 , peak periods T_p and main wave directions θ are collected for the period 2006–2016 at the model node with coordinates 41°.2708 N, 12°.9583 E, at around 77 m water depth, so that they can be assumed to be in deep waters. The same parameters are also collected for the period October 2017–March 2018, to be employed for the definition of XBeach wave input for the calibration stage.

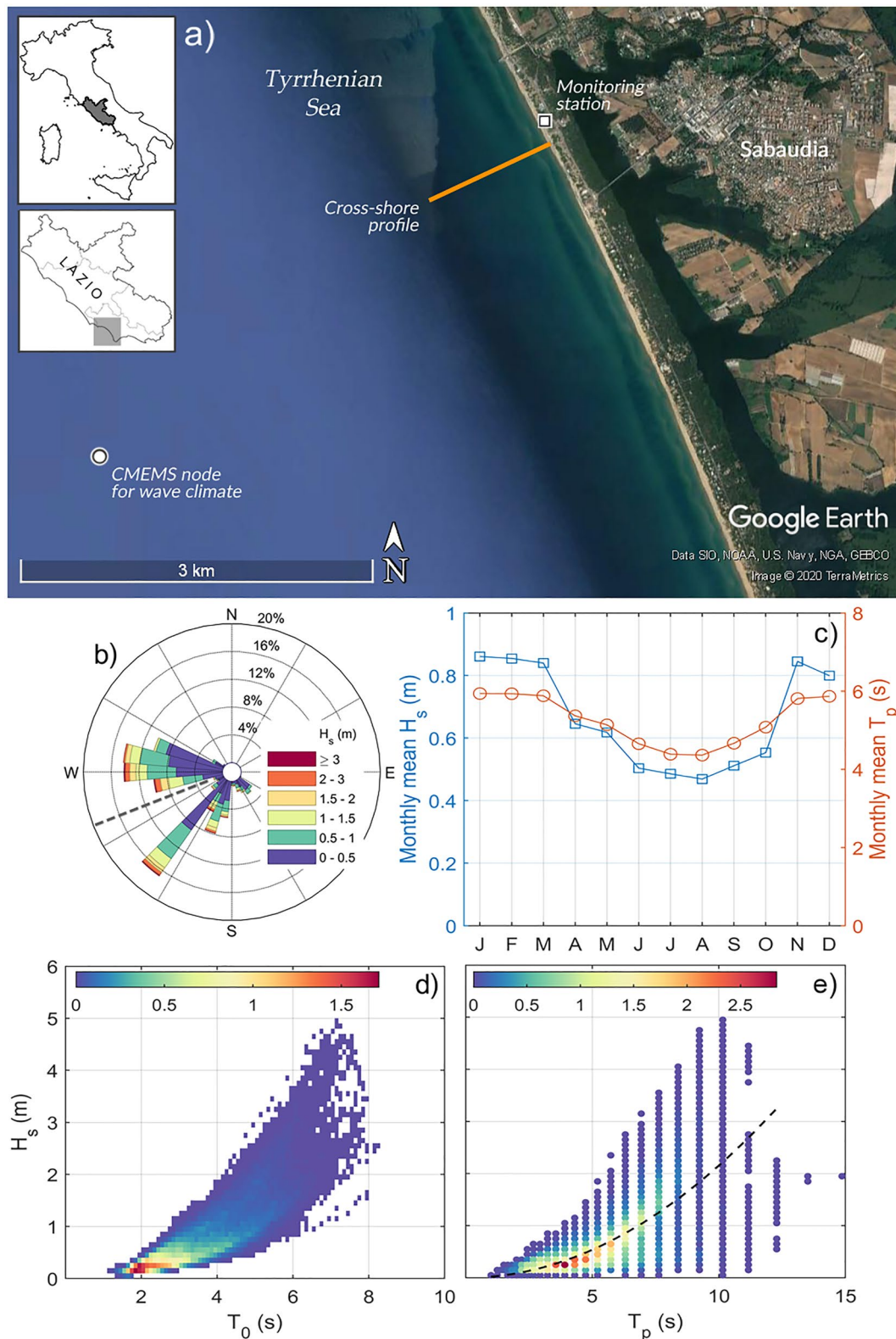


Figure 1. Geographical setting and hindcast wave climate (2006–2016) at Sabaudia. (a) Map of the Sabaudia coast (picture adapted from Google Earth). Locations of the video-monitoring station, the cross-shore profile used for the numerical simulations, and the CMEMS model grid node for wave parameters extraction are shown. (b) Directional wave rose; the normal direction to the coast is given with a dashed line; (c) monthly mean H_s (blue line) and T_p (orange line); (d) joint probability distribution of H_s-T_0 ; (e) joint probability distribution of H_s-T_p . The best fit regression line of Equation 1 is plotted with a dashed line.

Table 1
Significant Wave Height H_s , Peak Period T_p , and Dimensionless Fall Velocity Ω for the Six Sample Wave Events

Storm	S1	S2	S3	S4	S5	S6
H_s (m)	0.58	0.85	1.25	1.83	2.68	3.24
T_p (s)	5.21	6.30	7.63	9.23	11.17	12.28
Ω	6.7	8.1	9.8	11.9	14.4	15.8

A long-term wave climate characterization is given in Figures 1b–1e. Wave attack is predominantly bimodal in the area, with waves coming from the W and SW sectors (Figure 1b). The 10-year mean significant wave height is 0.66 m. Average wave parameters show marked seasonal variability in both wave height (monthly mean H_s up to 0.9 m in winter and around 0.5 m in summer months) and peak period (monthly mean T_p of 6 s in winter and 4.5–5 s in summer; Figure 1c).

Based on 2006–2016 modeled wave statistics, the Iribarren number $\xi = \beta_s / \sqrt{H_0/L_0}$ (Battjes, 1974), with β_s being the mean surf zone slope, ranges between 0.2 and 1 for weak-to-moderate wave conditions ($H_s < 2$ m)

but is consistently below 0.3, the threshold value for dissipative-state profiles (Soldini et al., 2013; Stockdon et al., 2006), for $H_s > 3$ m. This qualifies the morphological state of the beach as intermediate-to-dissipative (Wright & Short, 1984), such state shifting toward the dissipative end of the spectrum with more intense waves.

Estimated 10-year joint probability distributions of H_s-T_0 and H_s-T_p are given in Figures 1d and 1e. Figure 1e also shows the best fit curve of the dataset H_s-T_p , which gives the following site-specific empirical relation:

$$H_s = \left(\frac{T_p}{6.818} \right)^2 \quad \text{or} \quad T_p = 6.818\sqrt{H_s} \quad (1)$$

With $R^2 = 0.56$ significant at the 95% level. Equation 1 is used to define six wave events statistically representative of the 10-year hindcast, which are later used to evaluate long-wave transformation and beach response as a function of wave climate intensity (Section 3). H_s and T_p for the sample events are collected in Table 1, along with the respective dimensionless sediment fall velocity Ω . All selected events belong to lower-intermediate-to-dissipative states for the investigated beach ($\xi \approx 0.23$ and Ω above the threshold value of 6; Wright & Short [1984]) and are therefore suitable for a numerical study of wave evolution where breaking-related processes are involved.

The influence of tidal stage on infragravity energy fluxes is also investigated in this work. For this purpose, mean high water spring (MHWS) and mean low water spring (MLWS) levels are extracted from a 3-year tidal record from the nearby tide gauge at Anzio, about 36 km north-west of Sabaudia (Website of the Italian Tide Gauge Network, 2021), and given as uniform initial water level for the sample events in Table 1, allowing simulation of different tidal stages. MHWS and MLWS levels of +0.2 m and -0.2 m are obtained, respectively, confirming the microtidal nature of the investigated coast.

2.3. Video-Monitoring Products and Post-Processing

The beach of Sabaudia and the surrounding coast are being monitored since 2015 by a video-monitoring facility installed and maintained by the Italian Institute for Environmental Protection and Research (ISPRA). The monitoring station is installed on the roof of a building about 100 m from the shoreline, at an elevation of about 21 m above sea level. The horizontal and vertical fields of view are 57°.85 and 47°.63°, respectively, while the mean azimuth is 146°.33. The station captures snapshots of the nearshore in each daylight hour (Figure 2a) and produces typical products such as time exposure (timex) images, commonly used to track the evolution of submerged sand bars (Holman et al., 1993; Lippmann & Holman, 1989), and timestack images (Figure 2b) which can be profitably employed to study swash processes (Aagaard & Holm, 1989).

For the present application, swash properties at Sabaudia are extracted and employed to calibrate the model (see Section 2.4). Standard photogrammetric procedures were used to project the oblique video image onto a planar surface, coincident with the local sea level (Hartley & Zisserman, 2004; Holland et al., 1997). The geometrical solution of the projection was constrained with several ground control points and computed approximately weekly. All images were corrected for optical distortion following Bouguet (2004) and finally transformed into geometrically-correct plan views on a nominal 0.1 m grid; the resulting timestack track presents a cross-shore resolution ranging between 0.06 and 0.14 m (Figure 2). Timestacks are then analyzed to extract 15-min time series of the instantaneous shoreline at a mean frequency of about 2 Hz. The method employed for shoreline extraction, similar in nature to that of Vousdoukas et al. (2012), is based on a modified version of Otsu (1979)'s

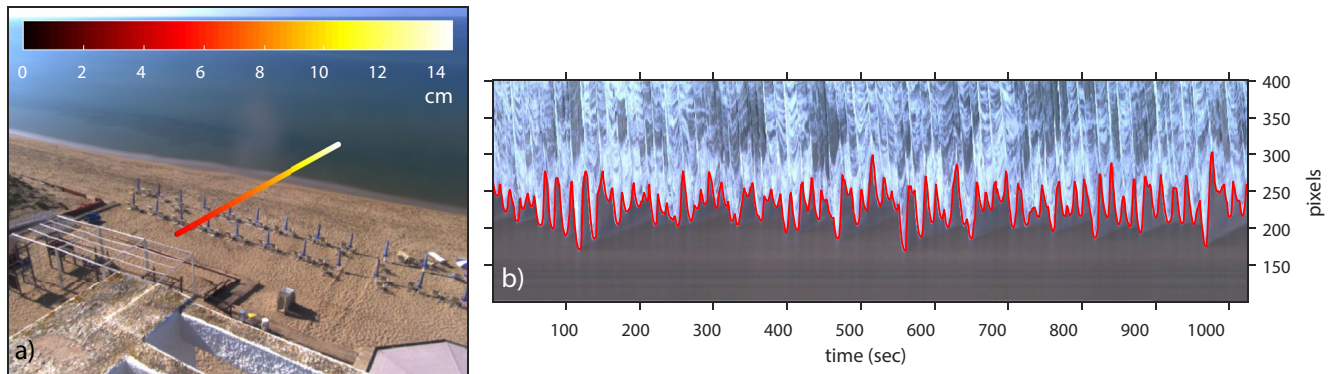


Figure 2. (a) Typical snapshot collected by the monitoring station. The line shows the section used for timestacks generation; colors show the variable pixel resolution of the section after image rectification and correction for lens distortion; (b) example of timestack. The extracted shoreline is highlighted in red.

threshold method and has been previously used for swash signal extraction (Valentini et al., 2019). A total of 1131 timestacks covering a 6-month period have been processed. Horizontal shorelines are then converted to real world coordinates. Conversion to run-up levels is made using the mean slope of the swash zone across a typical winter season ($\beta_{fw} \approx 0.07$), as obtained with statistical analysis of foreshore slopes from 19 measured seabed profiles in the period 2015–2020. Slopes have been evaluated as mean slopes between -0.5 m and $+1$ m from SWL for each profile. Unfortunately, as no directly measured cross-shore profiles were available in the investigated period, only an average based on a set of profiles could be assessed to obtain the most representative value of the foreshore slope.

Run-up time series are processed to single out individual swash events and their spectral energy density $\mathcal{E}(f)$ is evaluated to estimate the significant properties of the swash motion. Significant run-up height S and its components due to infragravity (low frequency) motions S_{IG} and incident (high frequency) waves S_{inc} is evaluated as follows:

$$S = 4 \sqrt{\int_{0.001 \text{ Hz}}^{0.5 \text{ Hz}} \mathcal{E}(f) df}, \quad S_{IG} = 4 \sqrt{\int_{0.001 \text{ Hz}}^{f_{sep}} \mathcal{E}(f) df}, \quad S_{inc} = 4 \sqrt{\int_{f_{sep}}^{0.5 \text{ Hz}} \mathcal{E}(f) df}, \quad (2)$$

where f_{sep} is the cut-off frequency between gravity and infragravity content, evaluated as a function of the respective H_s following the method by Oh et al. (2020):

$$f_{sep} = \begin{cases} 1/16.87 & \text{when } T_s \leq 7.5 \text{ seconds} \\ 1/(0.99 T_s + 9.44) & \text{when } T_s > 7.5 \text{ seconds} \end{cases} \quad (3)$$

where T_s is the significant period, calculated as $T_s = C \sqrt{H_s}$ with a mean value of $C = 4.3$ (Goda, 2000). The swash spectral centroids f_c , proxy for mean swash frequency, are evaluated as weighted mean of the frequency range from 0.001 to 0.5 Hz, with the spectral energy density $\mathcal{E}(f)$ as weights.

2.4. Numerical Modeling

XBeach is a process-based numerical model originally designed to simulate hydro-morphological processes on sandy beaches at storm-event scales (McCall et al., 2010; Roelvink et al., 2009) and recently used also to investigate flow properties in laboratory conditions (Ruffini et al., 2020) and to study the evolution of IGW (e.g., Bertin et al., 2020).

To make up for the lack of in situ hydrological data for Sabaudia, numerical simulations of nearshore wave propagation are performed by means of the one-dimensional non-hydrostatic (NH) implementation of XBeach, to calibrate the model against run-up levels from timestack analysis. In XBeach NH all short wave motions are

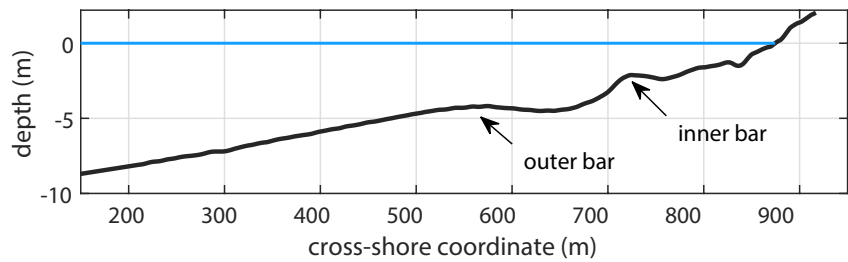


Figure 3. Bathymetric profile used for the simulations. The inner and outer bars are shown. The origin of cross-shore coordinates is placed at the offshore boundary of the profile.

explicitly resolved (Roelvink et al., 2009) and long wave (infragravity) generation and transformation processes are accounted for, which makes the model suitable for studies of low-frequency wave transformation.

2.4.1. Model Set-Up

The study cross-shore section (the location of which is highlighted in Figure 1a) is discretized into a 1D profile to be used as morphology input for XBeach. The bathymetric section chosen for the simulation campaign is an early-wintertime profile typical of the area, measured in 2019 (Parlagreco et al. (2019); see also Figure 1a), with an array of two sand bars on a mild surf zone beach ($\beta_s \approx 0.01$) and a steeper intertidal beach face with mean slope $\beta_f = 0.04$ – 0.045 . An inner prominent bar at about 2 m depth is located 150 m from the shoreline, while an outer, more subdued bar at 4 m depth is placed about 300 m from the shoreline (Figure 3). The real bathymetry has been surveyed from the emerged beach to 8 m depth, but to ensure that input waves are applied offshore of the “closure depth” to let them adjust to the local bathymetry before reaching the shore, it is artificially extended to a greater depth through a constant slope. Two maximum offshore depths, subjected to model calibration, are chosen: 10 and 15 m (see Section 2.4.2). These depths also serve as the offshore boundary of the model simulations, where wave input is applied. The chosen depth values fall within a range of depths commonly used in similar applications of nearshore modeling in XBeach (Cox et al., 2013; Matheen et al., 2021; Rutten et al., 2021).

The grid is devised to allow for computationally efficient simulations while guaranteeing an adequate spatial resolution for wave propagation and swash dynamics. A minimum of 30 nodes per wavelength and a minimum resolved wave period of 3.5 s are imposed. The resulting grid has variable spacing with a maximum $\Delta x = 2.3$ m at the offshore boundary and a minimum $\Delta x = 0.1$ m at the emerged beach.

Bed friction is implemented as a dimensionless friction coefficient c_D computed with a Manning formulation: $c_D = gn^2d^{-1/3}$, where g is gravity acceleration, d is the local water depth, and n is the Manning coefficient in $s/m^{1/3}$ (Soulsby, 1997). Manning’s formulation implies a dependence of bed friction on water depth and gives a more realistic condition than Chezy-like (depth-independent) formulations, especially for swash zone processes, for which the typical water depth is usually low. Although the XBeach default value for n is $0.022 s/m^{1/3}$, model performance is tested with different values of n , representative of beaches ranging from sandy to cobble-made (Benson & Dalrymple, 1967). The sediment transport module of the model is switched off so that only the hydrodynamics is modeled.

2.4.2. Calibration

We perform a calibration of both physical and operational XBeach parameters. Modeled 2% exceedance wave-induced run-up values $R_{2\%}$ are compared with concurrently observed run-up (extracted from timestacks) during eighteen 2-day time windows selected in the period October 2017 – April 2018. The time windows are chosen to encompass a variety of moderate-to-intense wave conditions.

To define the wave boundary conditions for the simulations, the deep-water data extracted at the CMEMS node (hourly significant wave height H_s and peak period T_p) are firstly shoaled according to linear wave theory up to 10 or 15 m, according to the simulation. Shoaled parameters are then used as input to define hourly JONSWAP spectra

to be applied at the offshore boundary of the domain. The JONSWAP spectra are automatically varied at the end of each simulated hour ($wbctype = jonstable$) to follow the hourly variation of wave climate from CMEMS. This allows for the modeling of time-varying wave conditions within a single simulation.

Multivariate calibration is run on three parameters: the maximum value of wave steepness for the onset of wave breaking ($maxbrsteep = 0.4, 0.6, 0.8$), the Manning friction coefficient ($bedfriccoef = 0.035, 0.045, \text{ and } 0.055 \text{ s/m}^{1/3}$), and the offshore depth (10 and 15 m). Calibration also on the offshore depth is considered, to account for the possibility of model output being dependent on the wave input depth. The set of parameters giving the best performance is then used for the subsequent modeling of the sample wave events given in Table 1. In the calibration process, the generation of random waves is switched off ($random = 0$) to avoid introducing a further source of randomness in the evaluation of modeled run-up. We have set the run-up gauge depth ($rugdepth$) at 0.1 m, in line with other applications on XBeach run-up extraction (Fiedler et al., 2015; Stockdon et al., 2014).

Model accuracy in predicting run-up and swash features is evaluated by means of error statistics: MAE (mean-absolute error), bias and the modified Willmott index of agreement D (Willmott et al., 2012):

$$mae = \frac{\sum_{i=1}^n |P_i - O_i|}{n}, \quad (4)$$

$$bias = \frac{\sum_{i=1}^n (P_i - O_i)}{n}, \quad (5)$$

$$D = \begin{cases} 1 - \frac{1}{2} \frac{\sum_{i=1}^n |P_i - O_i|}{\sum_{i=1}^n |O_i - \bar{O}|} & \text{when } \sum_{i=1}^n |P_i - O_i| \leq \sum_{i=1}^n |O_i - \bar{O}| \\ \frac{1}{2} \frac{\sum_{i=1}^n |P_i - O_i|}{\sum_{i=1}^n |O_i - \bar{O}|} - 1 & \text{when } \sum_{i=1}^n |P_i - O_i| > \sum_{i=1}^n |O_i - \bar{O}| \end{cases} \quad (6)$$

where P_i and O_i are predicted and observed values respectively, \bar{O} is the mean of observed values and n is the number of observations. MAE represents the average model error (in absolute value), whereas the bias highlights model overestimation or underestimation. D is an index of global model performance ranging from -1 to 1 , with -1 indicating total disagreement between predictions and observations, and 1 indicating total agreement.

2.4.3. Simulation and Processing of Sample Wave Events

The calibrated XBeach is finally employed to model wave transformation for the six sample wave events of Table 1, using the same seabed profile employed for the calibration stage (Figure 3). In each simulation, input waves at the offshore boundary are randomly generated from a time-constant JONSWAP spectrum with parameters H_s and T_p as given in Table 1. The simulated events last 2 hr (7,200 s) of run time. Outputs of wave surface elevation and shoreline oscillation are extracted at a frequency of 2 Hz for the second hour of simulation; the first hour is used as model spin-up and its output is discarded.

The IG fraction of the modeled surface elevation η_{IG} is extracted from the total wave field η in each simulated storm, by low-pass filtering with a cut-off frequency f_{sep} evaluated as per Equation 3.

A further decomposition of the IG signal into incoming ($\eta_{IG,in}$) and outgoing ($\eta_{IG,out}$) components is performed by applying the decomposition method by Guza et al. (1984), valid for long waves traveling in shallow waters:

$$\eta_{IG,in} = \frac{1}{2} \left(\eta_{IG} + u_{IG} \sqrt{d/g} \right), \quad \eta_{IG,out} = \frac{1}{2} \left(\eta_{IG} - u_{IG} \sqrt{d/g} \right) \quad (7)$$

where η_{IG} and u_{IG} are the IG surface elevation and depth-averaged cross-shore velocity, respectively.

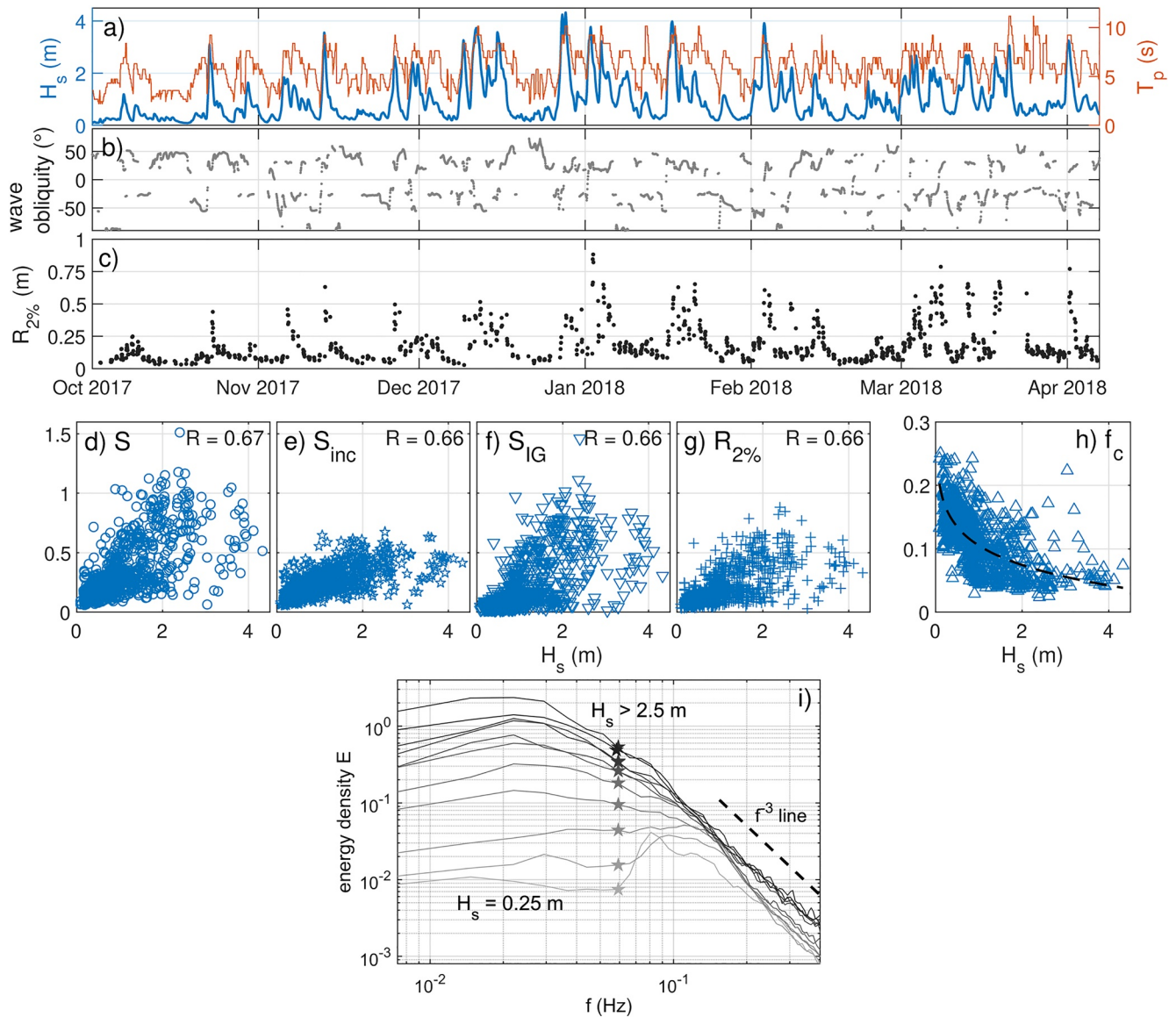


Figure 4. Comparison of wave climate parameters and run-up statistics for the period October 2017 – April 2018: (a) hindcast significant wave height H_s (blue line, left y-axis) and peak period T_p (orange line, right y-axis); (b) wave obliquity with respect to the shore normal; (c) run-up $R_{2\%}$ from timestack analysis. Scatter plots of (d) significant run-up height S , (e) incident run-up height S_{inc} , (f) IG run-up height S_{IG} , (g) run-up $R_{2\%}$, and (h) swash centroid frequency f_c against H_s (the best power-law fit is plotted as a dashed line). (i) Evolution of mean swash spectra for growing H_s . Swash spectra are binned according to H_s into 0.25 m-wide bins and ensemble-averaged. The stars mark the separation frequencies between gravity and infragravity modes, evaluated with corresponding H_s according to Equation 3. A f^{-3} -slope line is shown for reference.

3. Results

3.1. Real Swash Analysis

Run-up values $R_{2\%}$ extracted with timestack analysis are in good qualitative agreement with the wave climate hindcast extracted at the CMEMS node (compare black dots in Figure 4c with the blue line in Figure 4a). This gives preliminary confidence in using synthetic data as input for the model calibration in the lack of measured hydrodynamic data. Albeit with some unavoidable scatter due to the comparison of real and synthetic data sets, an agreement between modeled wave height H_s and resultant swash features is acceptable ($R = 0.67$ for total swash and $R = 0.66$ for swash components and run-up; Figures 4d–4g). The use of correlation coefficients here is not meant to imply a functional relationship between wave height and swash features, rather to confirm

the overall synchrony of synthetic, hindcast data, and real swash statistics; in other words, we wanted to check beforehand that, globally, high (hindcast) wave heights would correspond to high (observed) swash and run-up. The distribution of swash spectral centroids f_c (Figure 4h) shows that the mean swash frequency moves toward the low-frequency range as the offshore wave climate intensifies. This is also mirrored by binned and averaged swash spectra (Figure 4i) switching from a double-peak shape for low H_s , to single, wide peaks across the IG band for high H_s . This is indicative of a transition from a mildly reflective state in weak wave climate, to a distinct dissipative state for intense waves (e.g., see figure 1 in Hughes et al. [2014]). Swash spectra also display a clear f^{-3} roll-off band, indicative of short-wave energy saturation, which extends into the IG band for high H_s (Ruessink et al., 1998).

3.2. Model Calibration

Figures 5a–5i present a comparison between modeled (XBeach) and observed (timestacks) values of wave-induced run-up $R_{2\%}$ for varying combinations of the three calibration parameters. $bedfriccoef = 0.035$, the closest value to XBeach default settings, gives an overestimation of $R_{2\%}$ at high energy levels which reflects on the MAE (between 0.157 and 0.168 m), but overall yields virtually no bias (max bias of 0.04 m) and fair performance ($D = 0.559$ – 0.586 ; Figures 5a, 5d, and 5g). The Manning bed friction coefficient $bedfriccoef$ is the most influential in tuning model performance; a value of 0.045 slightly improves the overall skill (max D of 0.609 for offshore depth 10 m and 0.582 for offshore depth 15 m; Figures 5b, 5e, and 5h) and lowers the MAE to 0.149–0.162. Further increasing $bedfriccoef$ worsens the performance, especially for offshore depth of 15 m (Figures 5c, 5f, and 5i). Overall, model output is sensitive to offshore water depth, albeit the effect on D appears to be dependent on the specific combination of the other parameters.

Interestingly, $maxbrsteep$ has limited influence on model skill, especially for the medium and high values of $bedfriccoef$; this means that varying the breaking parameter influences the modeled $R_{2\%}$ to a very limited extent. However, $maxbrsteep$ is bound to have an impact on how breaking and, ultimately, surf zones are modeled. To benchmark model performance with the observed behavior in terms of wave breaking, we compare breaking patterns achieved by the optimal model setting ($rugdepth = 0.1$; $bedfriccoef = 0.045$; offshore depth 10 m) with $maxbrsteep$ of 0.4 (default value) and 0.6 (optimal value), with average first-breaking locations manually evaluated from timestacks for the six events defined in Table 1. Regarding modeled breaking, the percent of breaking time in Figures 6a and 6b is calculated as the fraction of the total simulation time for which a breaking wave is registered at a given cross-shore location. We take this parameter as a proxy for the presence of broken waves and to identify the modeled surf zone. As for observed breaking, timestacks whose corresponding offshore (hindcast) H_s falls within ± 0.1 m of the H_s of each wave event are gathered, their first-breaking location obtained, and finally treated statistically to give the box plot in Figure 6c. A better comparison might be accomplished by classifying breaking locations according to the offshore wave steepness in place of H_s ; however, this could not be achieved since the six events, evaluated as per Equation 1, have the same wave steepness.

It is observed that $maxbrsteep = 0.6$ gives unreasonably narrow surf zones even for moderate and intense wave states, with breaking seldomly modeled over the inner bar only for S5 and S6 (Figure 6b). Evidence of first breaking from timestacks, conversely, also places median breaking in event S4 approximately at the same cross-shore distance as S5 and S6 (Figure 6c), suggesting that breaking patterns (and surf zones) modeled with $maxbrsteep = 0.4$ may be more accurate. Given also that differences in D upon changing $maxbrsteep$ are minimal when $bedfriccoef = 0.045$ (0.599 vs. 0.609), we ultimately have decided to keep $maxbrsteep$ at the default value 0.4 for the sake of a more realistic outcome. Note that modeled cross-shore positions pictured in Figures 6a and 6b are different than the timestack-observed positions in Figure 6c: this is due to the former being evaluated by XBeach on a single profile (Figure 3), whereas statistics in Figure 6c are related to the period October 2017 – April 2018. Nonetheless, the comparison is useful to assess the accuracy of breaking patterns on a qualitative level, since the profile used for XBeach modeling is still representative of the nearshore of Sabaudia.

The performance of the optimal XBeach model ($rugdepth = 0.1$; $maxbrsteep = 0.4$; $bedfriccoef = 0.045$; offshore depth 10 m) is summarized in Figure 5j–m. The calibrated model, when coupled with hindcast input wave data from CMEMS, is able to reproduce swash features with reasonable mean accuracy. Modeled run-up $R_{2\%}$ is in good global comparison with real values with negligible global bias ($D = 0.6$, bias ≈ 0 ; Figure 5j). Comparison of real and modeled total swash S is also generally good, notwithstanding the scatter due to the coupling of real and

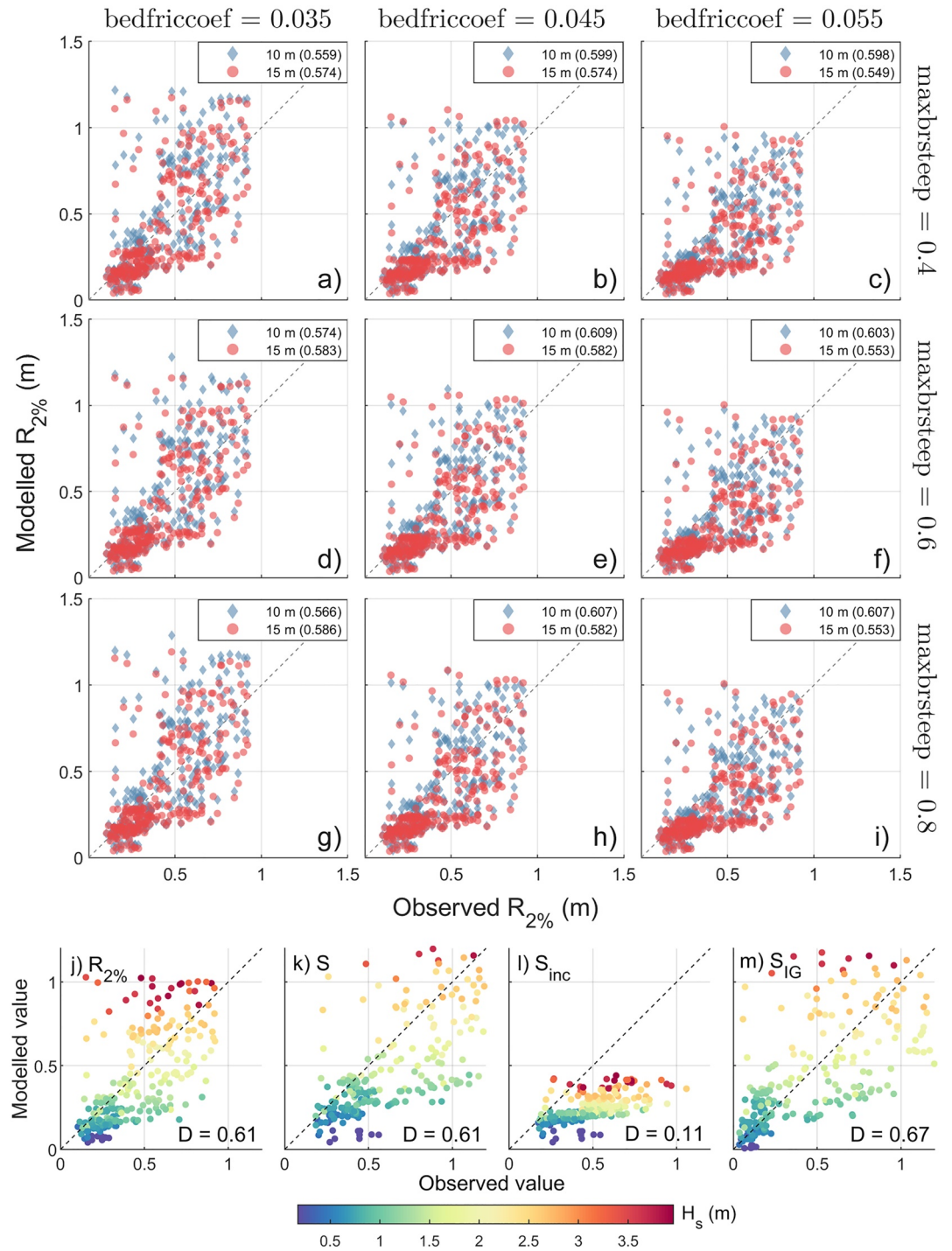


Figure 5. (a–i) Comparison of modeled versus observed run-up $R_{2\%}$ in the calibration tests, for different values of Manning friction coefficient (columns), maximum wave steepness parameter (rows), and offshore profile depth (blue diamonds vs. red circles in each panel). Willmott indices D are given in brackets in each legend. (j–m) Comparison of modeled versus observed parameters for the fully calibrated model. Each dot is color-coded according to the offshore H_s . Willmott indices D are shown in each plot.

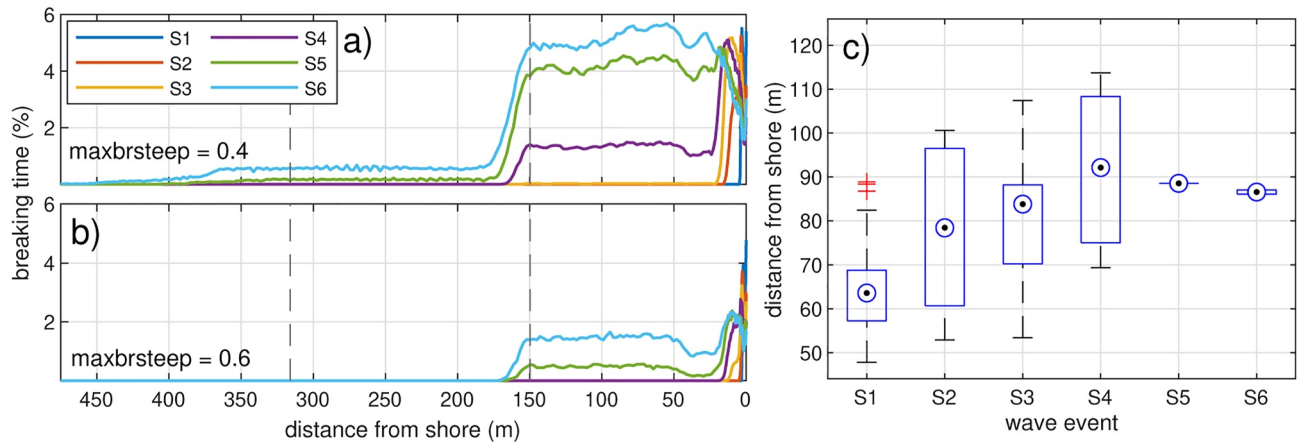


Figure 6. Comparison of breaking regions modeled by the calibrated XBeach with (a) $maxbrsteep = 0.4$ and (b) $maxbrsteep = 0.6$; the dashed vertical lines mark the position of inner and outer bars; (c) representative statistics of first breaking locations determined from timestacks for events S1 to S6. Dots mark median breaking positions.

synthetic data and a slightly negative bias ($D = 0.61$, bias = -0.11 m; Figure 5k). Predicted values of S_{inc} show the least agreement with the observed data, mainly due to the model generally underpredicting swash excursion in the incident frequency range, leading to a negative bias across the whole data set ($D = 0.11$, bias = -0.2 m; Figure 5l). On the other hand, the model shows fair performance in modeling the low-frequency swash component S_{IG} , albeit overestimating the real values, in particular for energetic wave conditions ($D = 0.67$, bias = 0.03 m; Figure 5m).

3.3. Wave Transformation Patterns for Sample Wave Events

The calibrated XBeach is employed to model the six sample wave events given in Table 1. Figures 7a–7c show the modeled evolution of significant wave height H_s , IG component $H_{s,IG}$, and breaking regions for the sample events.

Waves from the three least intense events (S1 to S3, $H_s < 1.3$ m) do not appear to break at the inner bar ($x = 720$ m; Figure 7c) albeit a drop in wave height is nonetheless modeled shoreward of it. The same events register a cross-shore increase in the IG fraction of wave height $H_{s,IG}$ across the shoaling phase (Figure 7b) simultaneously with a reduction of H_s . A mild rise and fall in $H_{s,IG}$ over the inner bar is observed for S3 (Battjes et al., 2004), whereas the growth rate for S1 and S2 is globally monotonic. Since breaking is modeled very close to the shoreline, this implies a gradual energy transfer from short-wave to IG frequencies by shoaling, as confirmed by bispectral analysis (see Section 3.4). On the other hand, events S4 to S6 ($H_s > 1.8$ m) exhibit variable breaking frequency over the inner bar. The most intense event S6 displays some occurrence of breaking even seaward of the subdued outer bar, starting at around $x = 500$ m. Such evidence places the inner bar at the seaward boundary of the surf zone during intermediate storms and well into the surf zone for the more intense sea states.

Modeled values of the short wave height $H_{s,SS}$ and IGW height $H_{s,IG}$ for specific cross-shore locations are shown in Figure 7d, along with best fitting power-law correlations ($H_{s,IG} = a H_{s,SS}^b$). Both in the shoaling zone ($x = 300$ m) and seaward of the inner bar ($x = 700$ m) the power-law correlation is close to the quadratic relation observed in field studies (Baldock & Huntley, 2002), with $b = 1.91$ and $b = 2.1$ respectively. However, shoreward of the inner bar and into the surf zone ($x = 760$ m) the model still gives a more-than-linear relationship with an increased exponent ($b = 3$), implying that IG motions gain more relative importance in the surf zone, as also observed on a barred beach by Ruessink (1998b).

Modeled patterns of total waves η and IGW ($\eta_{ig,in}$ and $\eta_{ig,out}$) for three sample events of increasing intensity are finally shown in Figure 8. IGW already present at the shoaling phase reaches the surf zone with changes in signal speed upon crossing the inner bar ($x = 720$ m; Figures 8b, 8c, and 8h). The change in speed is apparent by the change of wave rays slopes upon crossing the bar (see Figures 8b and 8c in particular) and is due to the sharp reduction in water depth between the seaward and landward sides of the inner bar (from about 5 to 2.5 m

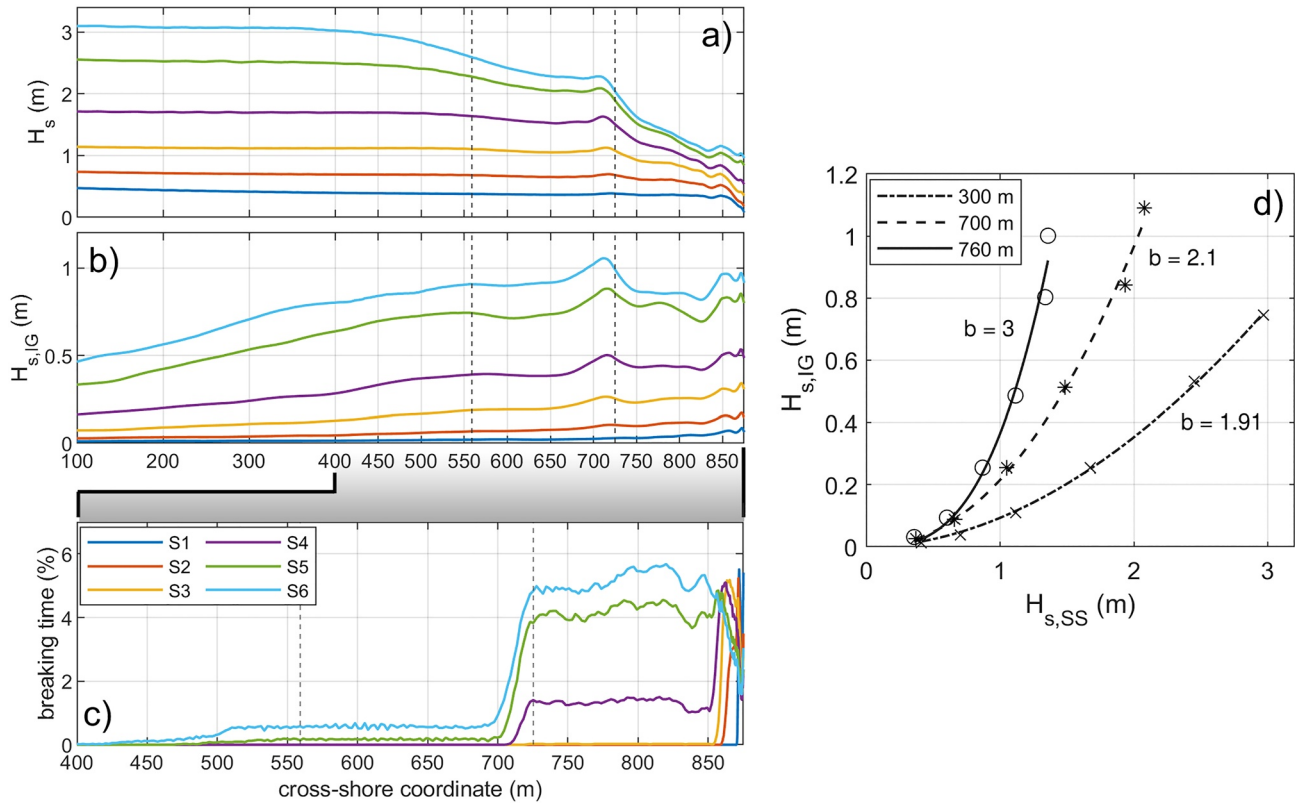


Figure 7. Modeled cross-shore evolution of (a) significant wave height H_s , (b) infragravity waves (IGW) height $H_{s,IG}$, and (c) surf zones width for the six sample wave events. *Note.* the different horizontal scale of panel (c) with respect to panels (a)–(b). The gray dashed lines mark the crests of the inner bar ($x = 720$ m) and outer bar ($x = 570$ m). (d) Relation between significant short wave height $H_{s,SS}$ and IGW height $H_{s,IG}$ at three cross-shore locations: $x = 300$ m (shoaling zone), 700 m (seaward of the inner bar), and 760 m (shoreward of the inner bar). Lines give best fits. Values of the exponents b of the power-law correlations are given for each line.

depth across 100 m; Figure 3). Local enhancement of the highest IG peaks and lowest IG troughs over the inner bar is also seldomly modeled, as shown by the intensification of red and blue hues upon crossing the inner bar in Figure 8e. IG signals are eventually reflected at the shoreline (Figures 8c, 8f, and 8i) and no generation of outgoing IGW at the breaking region, the signature of BFLW (Moura & Baldock, 2018), is registered. However, some asymmetry in both $\eta_{IG,in}$ and $\eta_{IG,out}$ is shown landward of the inner bar for the most intense event, apparent through dominance of red hues indicating positive IGW elevation (Figures 8h and 8i). This is due to storm setup caused by breaking waves (Longuet-Higgins & Stewart, 1964), which rises the mean water level in the surf zone. Seaward of the inner bar, the effect of storm setup is lost and IGW is again symmetric and, for outgoing waves, possibly regularized by deshoaling (Figures 8c, 8f, and 8i).

3.4. IGW as Group Bound Long Waves

IGW at Sabaudia are predominantly present as BLW as suggested by the more-than-linear relationship between IG and short waves (Figure 7d) and the absence of seaward-directed long waves generated at the breakpoint (Figure 8). Hereinafter we investigate BLW features using data from the modeled sample events.

As the wave train shoals, its IG content is carried as BLW (Longuet-Higgins & Stewart, 1964) in anti-phase with the short wave envelope ξ (Bertin et al., 2018). Cross-correlation between BLW and ξ at any given location in the shoaling zone should therefore yield negative peaks at near-zero lags (Moura & Baldock, 2017). Upon entering smaller depths, the BLW experiences a phase shift and lags behind the wave group as it receives energy from the short waves (Battjes et al., 2004), giving negative correlation peaks at positive lags. Finally, especially for the highest waves and upon breaking, positive surges preceding the BLW trough may occur due to

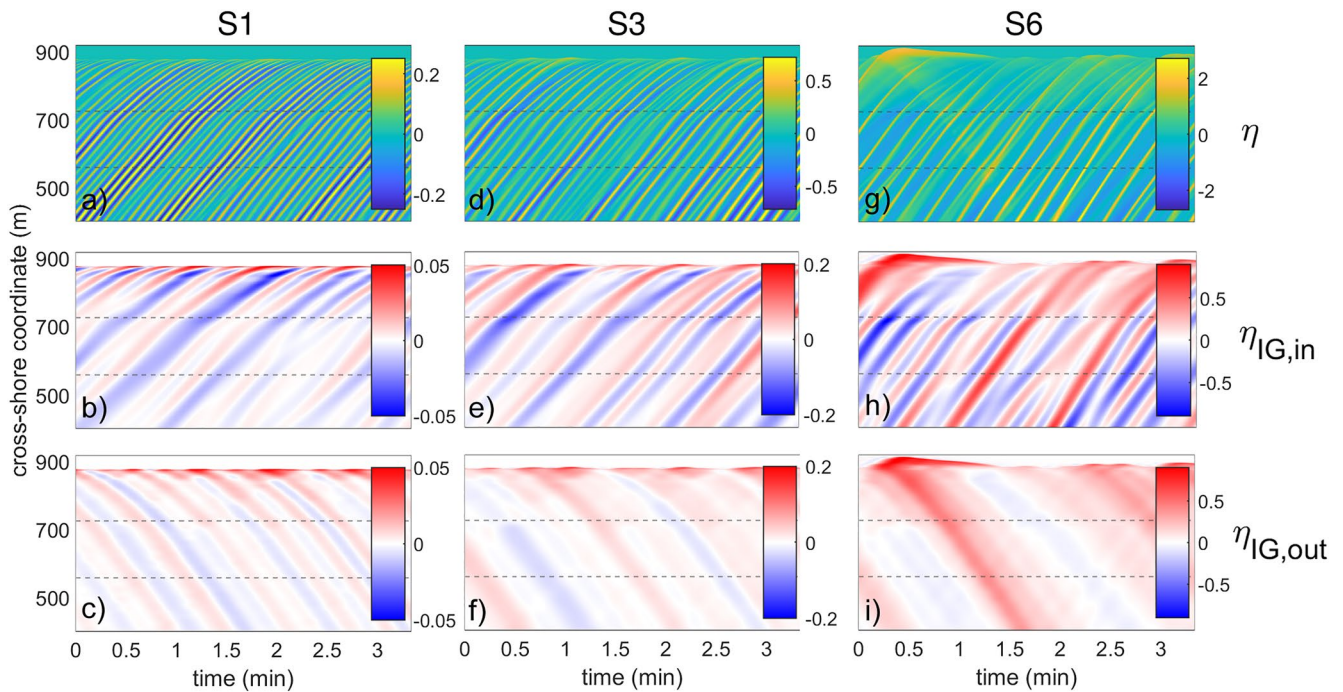


Figure 8. (a,d,g) Modeled total surface elevation η , (b,e,f) incident IG component $\eta_{IG,in}$, and (c,f,i) outgoing IG component $\eta_{IG,out}$ for sample events S1 (left column), S3 (middle column), and S6 (right column). Dashed black lines mark the locations of the inner and outer bars.

an excess of momentum flux. These surges appear as positive ξ - η_{IG} correlation peaks at negative lags (Moura & Baldock, 2017).

Figures 9d–9g illustrate ξ - η_{IG} correlations for four sample events at three cross-shore locations. The short wave envelopes ξ have been evaluated with the standard Matlab function used to extract peak envelopes. The correlations are performed over the second hour of each simulation after the first spin-up hour has been discarded. In the shoaling zone ($x = 400$ m; light blue lines) negative peaks at zero or near-zero lags suggest that BLW are still bound to the wave envelope. This is apparent for event S3, for which peaks in the envelope ξ and troughs in the IG fraction η_{IG} are in antiphase (top panel of Figure 9a). For the most intense storms (Figures 9f and 9g) mild positive correlations at negative lags (≈ 15 s) are related to a positive surge preceding the trough of the BLW (asymmetric bound wave; Moura & Baldock [2017]) and a phase shift, required for the energy transfer from short waves to take place (Battjes et al., 2004). This mechanism is visible in the time series of water elevation for event S6 at $x = 400$ m, where positive surges in η_{IG} (red circles) predate by ≈ 15 s the peaks of ξ (black squares; bottom panel of Figure 9a).

A change in correlation patterns occurs at the trough seaward of the inner bar ($x = 650$ m; medium blue lines), which corresponds to the outer surf zone for the most intense events (S4 to S6) and the inner shoaling zone for the other wave events. ξ - η_{IG} correlation is here positive at near-zero lag for event S6, suggesting that either the BLW is growing increasingly asymmetric (for waves still in the shoaling zone) or the IGW is no longer bound to the group and is propagating at the group velocity of the residual wave groups (for waves already broken in the surf zone). Mild waves, which have not yet experienced breaking at this location, still hold a negative correlation (Figure 9d), whereas intermediate storms (S3–S4; Figures 9e and 9f) begin to show a marked N-shaped correlation pattern (leading surge and lagging trough), much like event S6 exhibited in the shoaling zone.

Just seaward of the swash zone ($x = 850$ m; dark blue lines) only the mildest event S1 still exhibits a N-shaped correlation pattern typical of an asymmetric bound wave.

In conclusion, hints of BLW are apparent in the wave packet while still in the inner shoaling zone for all wave events. For the most energetic events, also a leading surge is identified through cross-correlation patterns. Upon entering the surf zone, the correlation quickly shifts to positive (with small or zero lags), except for the

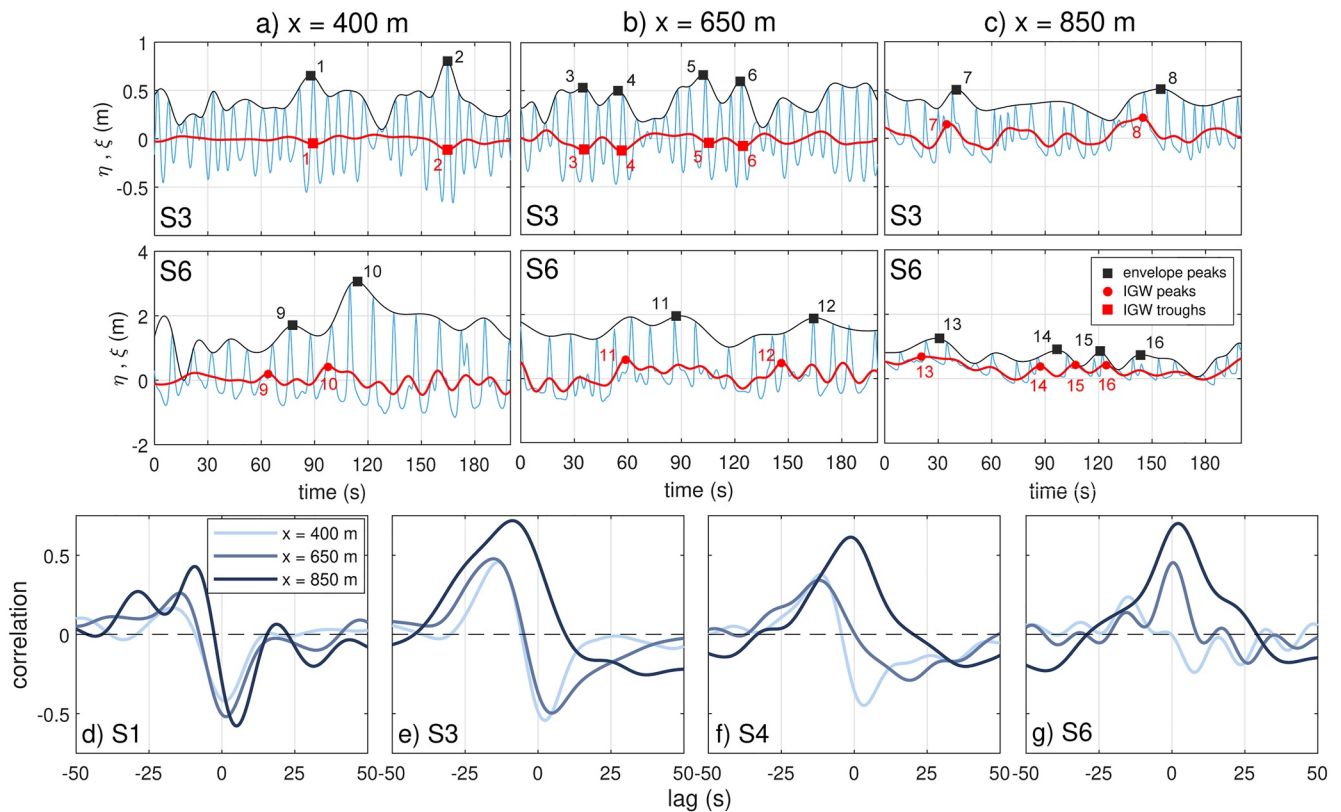


Figure 9. (a–c) Snapshots of wave trains η (light blue lines), short wave envelopes ξ (black lines), and infragravity waves η_{IG} (red lines) for sample events S3 and S6 at three cross-shore locations: $x = 400, 650$, and 850 m. IGW local peaks and troughs are marked with red circles and squares, respectively; envelope peaks are marked with black squares. (d–g) ξ – η_{IG} correlations for sample events S1, S3, S4, and S6 at the same locations.

mildest event, for which the breaking process occurs very close to the shoreline and no clear signal of released BLW is apparent while shoaling.

To complement the analysis, the energy exchanges between short waves and IG waves are discussed through bispectral analysis (Collis et al., 1998; Hasselmann et al., 1962). The bispectrum allows for the detection of phase coupling between triads of frequencies ($f_1, f_2, f_3 = f_1 + f_2$), a phenomenon responsible for nonlinear energy transfers among frequencies in an evolving wave field and, ultimately, the development of IGW (de Bakker et al., 2015; Bertin et al., 2020). Given a time series of surface elevation η , the bispectrum is evaluated as:

$$B(f_1, f_2) = \langle A_{f_1} A_{f_2} \overline{A_{f_1+f_2}} \rangle \quad (8)$$

where A_{f_1} , A_{f_2} and $\overline{A_{f_1+f_2}}$ are the Fourier coefficients of the wave components of η at frequencies f_1, f_2 , and $f_1 + f_2$, the bar symbol $\bar{\cdot}$ represents complex conjugation, and the braces $\langle \cdot \rangle$ indicate an ensemble mean. The imaginary part of the bispectrum, $B_I(f_1, f_2)$, gives information on the relative transfers of energy between phase-coupled frequencies.

Figure 10 shows the imaginary parts of bispectra evaluated for sample events S1, S3, and S5, at four locations spanning from the outer bar to close to the shore. Colors represent the direction of the energy transfer. Red hues at a point (f_1, f_2) mean a transfer from f_1 and f_2 to the sum frequency f_3 , that is, a redistribution of energy to higher frequencies. Blue hues represent a transfer from the sum frequency f_3 to f_1 and f_2 , that is, a transfer from high to low frequencies. Frequency axes are scaled with the frequency peak f_p of each event, so that all spectral peaks correspond to $\hat{f} = f/f_p = 1$.

As can be seen, the largest frequency ξ interactions are identified in locations inside the shoaling zone for all events. In the mildest event S1, for which shoaling is modeled up to some 20 m from the shore, frequencies around the

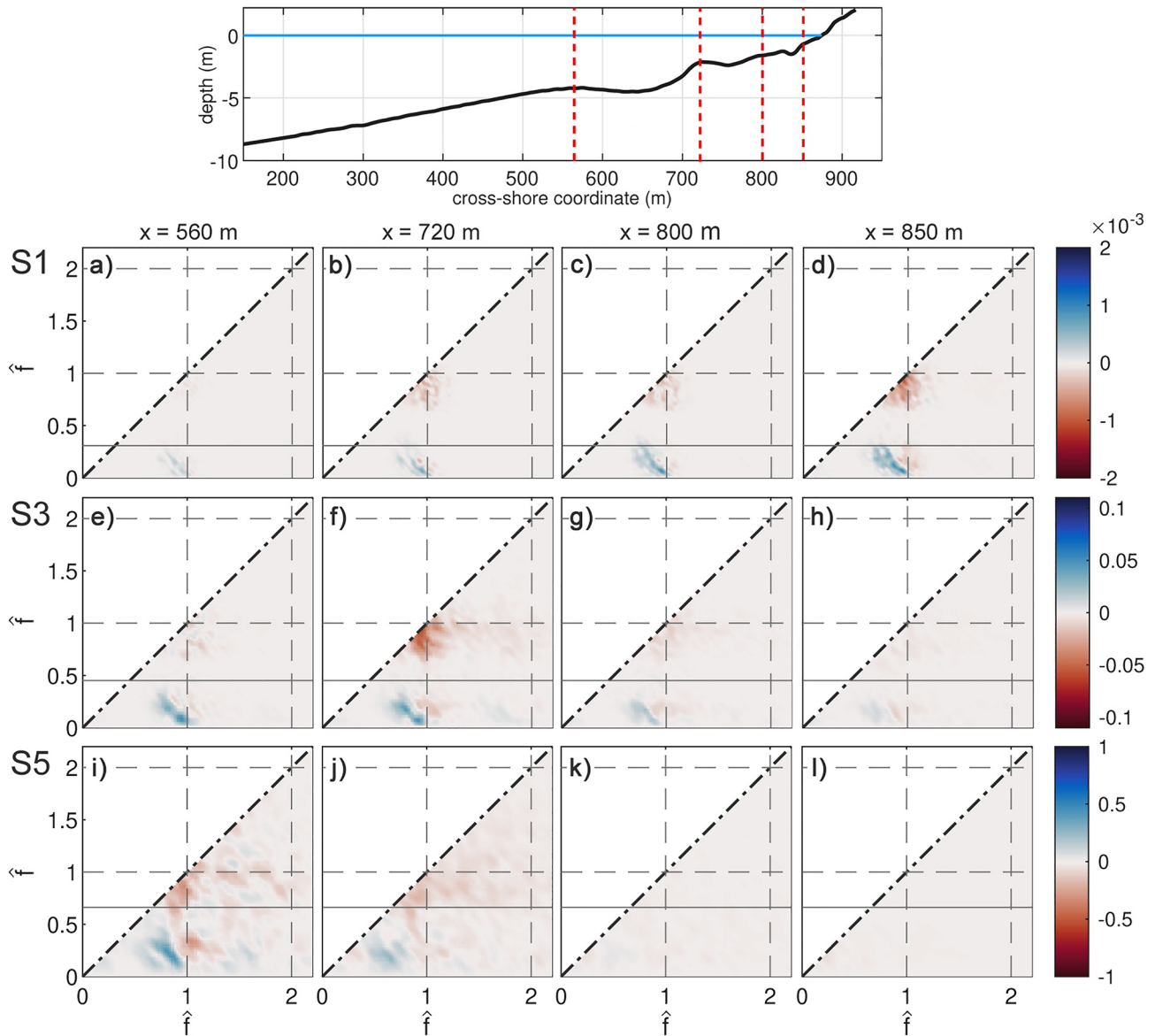


Figure 10. Imaginary part of the bispectrum evaluated for (a–d) event S1, (e–h) event S3 and (i–j) event S5 at several cross-shore locations: $x = 560$ m (top of outer bar), 720 m (top of inner bar), 800 m (inner surf zone) and 850 m (close to the shoreline), as a function of dimensionless wave frequency $\hat{f} = f/f_p$. The thin horizontal solid lines mark the separation between short and IG waves, f_{sep}/f_p . The cross-shore profile is shown in the top panel. The four chosen locations are marked with red dashed lines.

peak continuously distribute energy to superharmonics shoreward of the inner bar, $x > 720$ m (red hues around $(\hat{f}_1, \hat{f}_2) = (1, 1)$), indicating a growing wave skewness. At the same time IGW receive energy from the spectral peak (blue hues with peaks at $(\hat{f}_1, \hat{f}_2) = (0.95, 0.07)$ and $(0.86, 0.13)$; Figures 10b–10d). Only very close to the shoreline, $x = 850$ m, also a hint of energy reversal from IG frequencies back to the peak is seen (red hues at $(\hat{f}_1, \hat{f}_2) = (0.93, 0.16)$; Figure 10d).

For intermediate event S3, the same behavior observed in event S1 is shifted seaward, the largest interactions now being observed in proximity of the inner bar, $x = 720$ m. BLW receive energy from frequencies around the peak (blue hues with peaks at $(\hat{f}_1, \hat{f}_2) = (0.95, 0.07)$ and $(0.86, 0.13)$; Figures 10e and 10f) in cross-shore locations still lying into the shoaling zone. Only in the surf zone, $x \geq 800$ m, residual interactions are noticeably smaller, the sign of short wave dissipation and BLW release (Figures 10g and 10h).

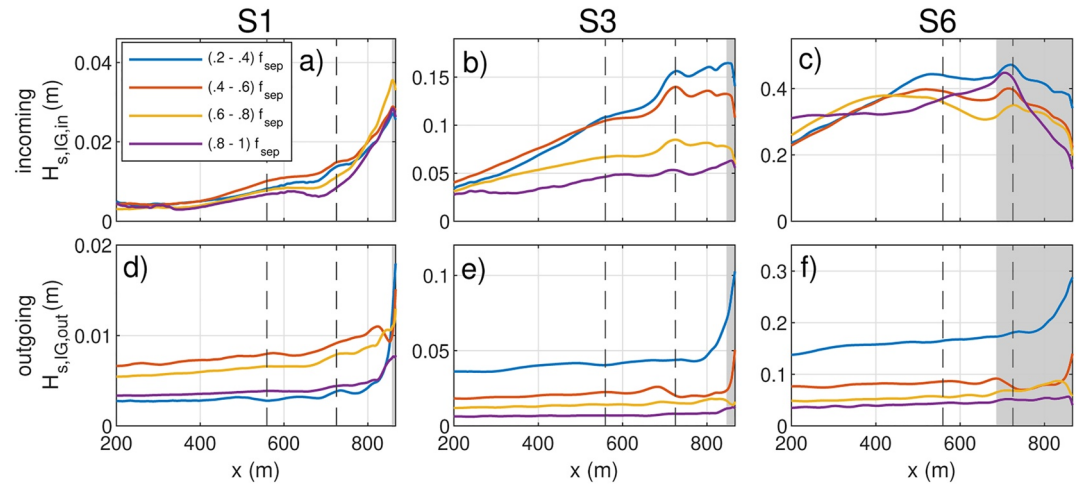


Figure 11. (a–c) Frequency-dependent incident infragravity wave (IGW) height $H_{s,IG,in}$ and (d–f) outgoing IGW height $H_{s,IG,out}$ for sample wave events S1, S3, and S6. Dashed vertical lines mark the crests of the inner and outer bars. Gray regions highlight zones of dominant breaking according to modeled surf zones given in Figure 7c. Note the different scales for the vertical axes.

Finally, for intense event S5 the bulk of energy transfers is detected further offshore, mainly around the outer bar (blue hues in a strip around $(\hat{f}_1, \hat{f}_2) = (0.83, 0.29)$; Figure 10i), concurrently with some energy reversal back to above-peak frequencies (red hues at $(\hat{f}_1, \hat{f}_2) = (1.05, 0.35)$). Residual transfers are modeled also over the inner bar, where receiving IGW frequencies are downshifted (blue hues at $(\hat{f}_1, \hat{f}_2) = (0.6, 0.2)$; Figure 10j). Interactions in the IG band are again absent in the surf zone, which indicates BLW release (Figure 10k–l).

3.5. Frequency Dependence of IGW and Tide Effects

To assess the frequency dependence of infragravity processes, the heights of incident ($H_{s,ig,in}$) and outgoing IGW ($H_{s,ig,out}$) are calculated for IG bands whose limits are given as fractions of f_{sep} . Results are given in Figure 11. The incoming IG height ($H_{s,ig,in}$; Figures 11a–11c) displays more or less pronounced maxima over the inner bar. Increases over the bar are the same in magnitude across all IG bands, implying that the IG response to reducing depths over the bar is frequency-independent in our case. For outgoing IGW ($H_{s,ig,out}$; Figures 11d–11f) maxima over bars are not apparent, as also observed by Battjes et al. (2004). The reduction of IGW heights upon reaching the inner bar (apparent for event S6; Figure 11c) signals that low-frequency motions are not coupled with the short waves and are free to propagate and dissipate by, for example, IGW breaking (Ruessink, 1998a). IGW growth landward of the inner bar is somewhat hindered at all IG bands also in event S3 (Figure 11c), even though at this location the low-frequency motions should still be BLW according to the model. This fact may be explained by IG frequencies exchanging energy with swell-sea frequencies over the inner bar (Figures 10f and 10g) and preventing further growth of IG heights. Finally, although small in comparison, IGW grows unimpeded by an order of magnitude with respect to the offshore value until the very narrow surf zone in the mild event S1 (Figure 11a), as typical for bound waves (Ruessink, 1998a).

Differences between frequency bands arise when IG reflection patterns at the beach face are investigated by means of the amplitude reflection coefficients R^2 across the surf zone and near the shoreline (Sheremet et al., 2002). R^2 close to one indicates strong reflection at the shore, generally associated with a relatively steep beach face and small IG dissipation in the inner surf zone. Small R^2 , conversely, denote less IG reflection, by either dissipation of low-frequency waves across the surf zone or through swash processes over a gentle swash zone. R^2 is defined as the ratio between outgoing (F^-) and incoming (F^+) low-frequency energy fluxes:

$$R^2 = \frac{F^-}{F^+}. \quad (9)$$

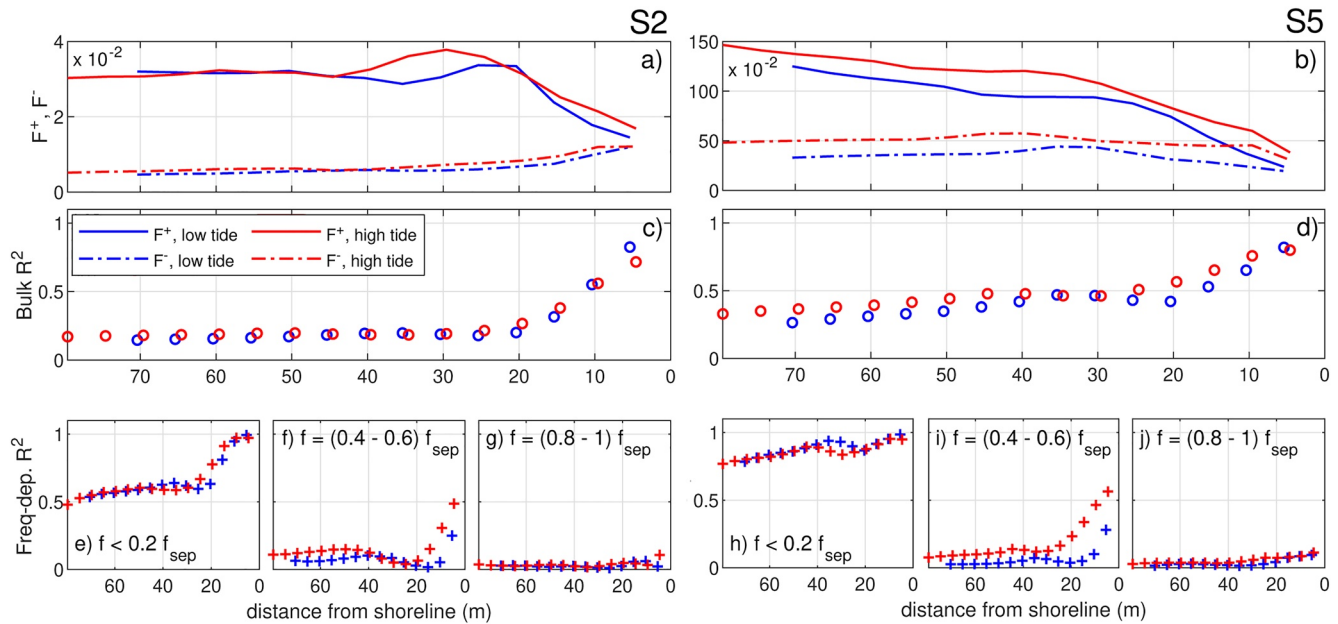


Figure 12. (a, b) Modeled inner surf zone evolution of incoming (F^+ , solid lines) and outgoing IG fluxes (F^- , dash-dotted lines); (c, d) bulk IG reflection coefficients R^2 ; (e–j) frequency-dependent IG reflection coefficients, for sample wave events S2 (left panels) and S5 (right panels), at low tide (MLWS = -0.2 m; blue lines and symbols) and high tide (MHWS = $+0.2$ m; red lines and symbols). Please note the different scales for the fluxes in panels (a, b).

F^+ and F^- for the whole IG band ($f < f_{\text{sep}}$) and for specific sub-bands, whose intervals are defined as fractions of f_{sep} , are evaluated from modeled cross-shore fields of detrended water surface elevation η and flow velocity u at any given cross-shore location, by applying the co-located method by Sheremet et al. (2002):

$$F^{\pm} = \int_{f_{\text{min}}}^{f_{\text{max}}} \mathcal{F}^{\pm}(f) df, \quad (10)$$

$$\mathcal{F}^{\pm}(f) = \frac{\sqrt{gh}}{4} \left\{ C_{\eta\eta}(f) \pm 2\sqrt{\frac{h}{g}} C_{\eta u}(f) + \frac{h}{g} C_{uu}(f) \right\}, \quad (11)$$

where h is water depth, g is gravity acceleration, $[f_{\text{min}} f_{\text{max}}]$ is the frequency range over which the fluxes $\mathcal{F}^{\pm}(f)$ are to be integrated, $C_{\eta\eta}$ and C_{uu} are the water elevation and flow velocity autospectra, respectively, and $C_{\eta u}$ is the η – u cospectrum, that is, the real part of the η – u cross-spectrum. Bulk IG reflection coefficients are evaluated by integrating the fluxes over the whole IG band, while band-specific coefficients are integrated across each sub-band.

Figure 12 shows the distribution of modeled fluxes F^{\pm} and IG reflection coefficients R^2 for two sample wave events of different intensities, representative of mild and intense wave climate, at conditions of low and high tide. F^{\pm} and R^2 are evaluated by means of Equations 9–11 at a set of cross-shore locations in the inner surf zone (up to about 80 m seaward from the mean still-water shoreline). To compare low- and high-tide observations in a single reference frame, all data are plotted as a function of the distance from the respective undisturbed shoreline. Bulk reflection is generally high in the innermost portion of the surf zone ($R^2 > 0.5$ at 10–20 m from the shoreline, $d \leq 1$ m) and decays seaward with stronger gradients for mild than for intense wave climate (Figures 12c and 12d). The lowest IG frequencies, $f < 0.2 f_{\text{sep}}$, experience the largest reflection (Figures 12e and 12h) with surf zone R^2 consistently over 0.5 for mild event S2 and over 0.7 for energetic event S5. As the IG frequency increases toward the short-wave range, the modeled reflection coefficients decrease and eventually become negligible, indicating increasingly dominant dissipation at the shore (Figures 12g and 12j). Although showing similar trends, incoming fluxes F^+ are larger at high tide than at low tide (Figures 12a and 12b) due to slightly larger water depths contributing in reducing energy losses from frictional dissipation and/or wave breaking. Tidal modulation of F^+ is also mirrored by different levels of offshore F^- , even though with intense wave climate only, as observed also by Thomson et al. (2006).

4. Discussion

4.1. Hindcast Data as Input for Numerical Modeling

In the present work, we have explored the possibility of using hindcast data from the oceanographic service CMEMS as input for the calibration of XBeach against observed swash properties. Wave data from CMEMS have been previously used to study sandbar displacement patterns with good results (Melito et al., 2020).

Good correspondence between hindcast wave climate and real swash properties across a 6-month period ($R = 0.66$ – 0.67 ; Figures 4d–4g) supports the use of data from CMEMS in conjunction with XBeach for swash modeling. Nonetheless, some scatter is observed between modeled (obtained by XBeach using hindcast wave parameters as input) and real swash features, due to the different nature and not always exact correspondence of the data sets. This is all the more apparent for S and S_{IG} (Figure 5k,m) and results in MAE of 0.2 m for both statistics. On the other hand, performance on run-up is good, with $D = 0.61$ and a MAE of 0.14 m.

Calibration has been made upon swash-zone properties, which are the final product of a series of complex hydrodynamic processes (shoaling, breaking, frictional energy loss) taking place across the surf zone. Calibration on real, measured hydrodynamic parameters would likely yield a physically grounded model tuning and reduce errors; nonetheless, we deemed it interesting to investigate a new line of approach in which only low-cost and free data are available. This would prove useful—or even inevitable—in cases where model calibration is desired, but the deployment of in situ instrumentation for the collection of real data is troublesome, not economically convenient, or impossible.

4.2. Model Performance

The 1D version of the non-hydrostatic XBeach with default parameters slightly overestimates run-up $R_{2\%}$, with the highest overestimation occurring for high-energy conditions (Figure 5a), as observed also by Stockdon et al. (2014). As expected, friction is shown to have a major influence on improving average model performance (Conde-Frias et al., 2017), with higher Manning coefficients reducing modeled $R_{2\%}$. Although the default value for the run-up gauge depth is 0.005 m, a larger value of 0.1 m has been fixed during calibration, consistently with other studies (Fiedler et al., 2015; Pinault et al., 2020; Stockdon et al., 2014) which used the same value to extract run-up from lidar timestacks and numerically modeled swash.

A negative bias for S_{inc} means a global underprediction of incident swash and might suggest that the default wave dissipation formulation implemented in XBeach gives an energy dissipation higher than that observed in the field, irrespective of tuning parameters. The model also shows a clear saturation value of about 0.45 m for S_{inc} (Figure 5l) and less scattering around the respective observed values, although the saturation value for S_{inc} is higher for observed swash motions (0.8 m). On the other hand, modeled IG swash S_{IG} shows virtually no sign of saturation (Figure 5h), as confirmed also by growing energy in the IG range from remotely sensed swash spectra, except for the most intense waves for which the highest IG frequencies experience incipient saturation (Figure 4e). Swash saturation at the highest IG frequencies (down to 0.035 Hz) has been also documented by Senechal et al. (2011) during extreme oceanic wave conditions, suggesting this as typical behavior for low-sloping beaches, regardless of absolute wave intensity.

Less scattering and comparable skill for predictions of $R_{2\%}$ than for S and S_{IG} (Figure 5) lend support to the choice of $R_{2\%}$ as the best parameter to be taken as an output from numerical models when forced by synthetic input data from oceanographic models, since its value is less influenced by individual waves than swash-related statistics are, at least in a long-term simulation.

4.3. IGW Evolution

IGW at Sabaudia are dominated by BLW, as commonly observed on gently sloping beaches (Baldock, 2012; Battjes et al., 2004). Long waves grow in intensity with all wave conditions as gravity waves undergo shoaling, with amplification ratios higher for milder waves (Figure 8). Upon reaching the surf zone and shoreline, their presence and intensity are still relevant to the point of quickly overcoming short-wave wave energy. Low-frequency energy accounting for up to 30% of the total energy at the shore of a barred model beach is observed by, for example, Van Gent and Giarrusso (2005). The IG height $H_{s,IG}$ is indeed in quadratic dependence from the

incident short wave height $H_{s,SS}$ in the shoaling zone (Figure 7d), hinted at by power-law correlation exponents around 2 (Baldock & Huntley, 2002); in contrast with, for example, Moura and Baldock (2017), however, such relationship is conserved and intensified in the surf zone, denoting that IGW experience little dissipation immediately after short wave breaking. This also highlights the irrelevance of breakpoint forcing, which is conversely dominant on steeper beaches, $\beta_s \approx 0.01$ or higher (Baldock et al., 2000; Pomeroy et al., 2012), especially when combined with steep waves.

IGW growth is hindered, although not completely stopped, upon crossing the inner bar for intermediate states and also the outer, subdued bar for the most energetic states (Figure 11b). The regions of IGW stationarity/decay are consistent with the identification of surf zones made through the identification of wave breaking regions (Figure 7), suggesting that the energy transfer from gravity waves to lower subharmonics, apparent during shoaling, is interrupted in the surf zone (Battjes et al., 2004) where the BLWs are finally released as free waves. This is confirmed by the bispectra not showing any meaningful interaction beyond the modeled points of wave breaking (Figure 10). $\xi-\eta_{IG}$ correlations are seen to shift from negative peaks to N-shapes or positive peaks (at zero or negative lags) as waves approach the surf zone for intermediate wave states (Figures 9e–9g), concurrent with the development of an asymmetric wave with a leading positive elevation as a result of dynamic setup. Our study confirms the presence of asymmetric IGW in the surf zone also in mild, barred beaches, much similar to what laboratory evidence (Baldock, 2006) and numerical modeling (Pomeroy et al., 2012) have previously observed on steep beaches and reefs. Moreover, bispectral analysis has revealed that IGW growth in the inner shoaling zone occurs simultaneously with a redistribution of energy from the range $(0.7-1)\hat{f}$, which covers peak and swell frequencies (Figures 10d, 10f and 10i). This observation agrees with the hypothesis that infragravity growth is forced by non-breaking, regularized swell waves (Herbers et al., 1995).

Dissipation by IGW breaking appears to be the dominant energy draining process for intermediate and intense wave states, as suggested by the decay of IG heights in the surf zone (Figures 11b and 11c), where the typical cross-shore distances are too short for seabed friction dissipation to be effective. This assumption is corroborated by still high IGW heights, reaching as much as 1 m before the shoreline (Figure 7b); IG wave heights of similar magnitude have been also reported by Guza and Thornton (1982), Ruessink et al. (1998), and Inch et al. (2017). Breaking dissipation in shallow waters (0.7 m) and short distances (25–55 m), likely promoted by IGW breaking seaward of the shore, is also observed at the similarly sloped beach of Ameland by de Bakker et al. (2014). Finally, no loss of IG energy due to transfer back to the incident band (Thomson et al., 2006) is apparent, since no triadic interactions from IG back to higher frequencies are modeled close to shore regardless of wave intensity ($x = 850$ m; Figure 10d,h,l). Interestingly, a back transfer from IGW to near-peak frequencies is modeled while still in the shoaling phase (Figures 10d, 10f, and 10i), suggesting that IG motions may give a portion of their energy back to swell-sea waves before they are released.

High values of R^2 at the shallowest region, up to 10 m from the shoreline (Figures 12c and 12d) and the growing relevance of IG energy in real swash spectra (Figure 4i) suggest that localized IG dissipation at the shoreline, by either swash interactions or depth-limited dissipation, may be limited; however, the modeled decay pattern of surf zone IGW heights for the moderately intense events (Figures 11b and 11c) is consistent with that obtained by SWASH simulations with a friction coefficient $c_f = 0.005$ in de Bakker et al. (2014), therefore we cannot completely rule out the effect of seabed friction into IGW dissipation, at least very close to the shore. The data in our study, unfortunately, does not allow us to further inspect the influence of dissipation mechanisms. A more complete understanding of the processes at hand would benefit from a collection and analysis of field observations.

4.4. Frequency and Tide Dependence of IGW Processes

Several studies have ascertained that the cross-shore transformation of low-frequency oscillations is a function of wave frequency (e.g., de Bakker et al., 2014; Battjes et al., 2004; van Dongeren et al., 2007). In Sabaudia, differences between IG bands are found mainly for moderate-to-strong wave conditions, with the lowest IG frequencies presenting the largest incident wave heights (Figures 11b and 11c) as well as the largest reflection (Figures 12d and 12h), while the higher IG frequencies are characterized by smaller heights and lower reflection. This behavior is connected with enhanced near-shoreline dissipation experienced by higher IG frequencies, since swash energy saturation (typical of gravity waves in the swash zone of a mild sloping beach) reaches the higher IG frequencies as wave climate intensifies (Figure 4i). Weak wave climate, on the other hand, yields a continuous growth of

low-frequency content up to the shoreline at all frequencies, likely due to the limited influence of wave breaking and seabed dissipation, and still non-negligible reflection at the lowest frequencies (Figure 12e).

A modified version of the dimensionless normalized bed slope (Battjes et al., 2004), developed with a focus on infragravity frequencies, can be profitably used to discuss dissipation and reflection of IGW in very shallow waters (de Bakker et al., 2014; van Dongeren et al., 2007):

$$\beta_H = \frac{d_x}{2\pi f_{IG}} \sqrt{\frac{g}{H_{IG}}} \quad (12)$$

where d_x is the bed slope, f_{IG} is the IG wave frequency, H_{IG} is the incoming IGW height at a given point close to the shore. Using β_H , two regimes can be distinguished (Battjes et al., 2004): (a) a *steep-slope regime*, in which IGW experiences little-to-no dissipation and considerable reflection occur at the shore and (b) a *mild-slope regime*, where IGW dissipation is more consistent, likely due to breaking of IG bores very close to the shore.

Our findings mark a difference from the literature in regards to regime transition. Normalized bed slopes evaluated at $x = 850$ m ($d = 0.75$ m, mean bed slope of 0.04) give values of 3.22–9.25 across all IG bands for the mildest event S1, which indeed presents a steep-slope behavior with virtually no dissipation of the incoming IG energy (Figures 11a and 11d). On the opposite side of the spectrum, $\beta_H = 0.94$ –2.05 is predicted for the most energetic event S6, presenting a distinct mild-slope regime with consistent IG dissipation onshore of the inner bar for all frequency bands ($x > 700$ m; Figures 11c and 11f). The intermediate state S3 shows a combination of features: shoaling of IG waves up to the inner bar and stationarity shoreward of it (Figures 11b and 11e). This case lies in the transition range between the two regimes and yields $\beta_H = 1.83$ –3.98; such range of values is higher than classical thresholds identified through analysis of experimental data, $\beta_H \approx 1$ –1.25 (Battjes et al., 2004; van Dongeren et al., 2007). Our findings thus go in favor of the concept of regime transition occurring for values of β_H higher than those suggested by the literature. In fact, our result is more compatible with the tentative threshold $\beta_H \approx 3$ suggested by de Bakker et al. (2014) and found for a slope of 0.0125.

Although in a distinctly microtidal environment, the effect of the tide is apparent in altering onshore energy fluxes and reflection coefficients, mainly for intermediate IG frequencies (Figures 12f and 12i). Those frequencies are at the transition between a steep-slope regime with predominant reflection (low IG frequencies) and a mild-slope regime, where dissipation is dominant (high IG frequencies), so tidal excursion is effective in shifting the boundary between the almost complete reflection at lowest IG, and the dominant dissipation at highest IG, even though the tide is not seen to exert a significant influence on the bulk IGW reflection (Figures 12c and 12d). Specifically, low tide reduces reflection of the intermediate IG mainly by reducing F^+ close to shore (thus shifting the beach behavior toward a mild-slope regime for that frequency band) and leaving much less energy to reach to shoreline and be reflected (Thomson et al., 2006). Although different in value, decreasing rates of F^+ are similar in high tide and low tide (Figures 12a and 12b), due to almost equal surf zone and intertidal beach slopes at high and low tide.

5. Conclusions

A numerical analysis of the generation and transformation of low-frequency waves at the dissipative, microtidal beach of Sabaudia (Tyrrhenian Sea, Italy) has been proposed. IG evolution patterns originating from a range of wave conditions and tidal stages are investigated. The study contributes to increasing our understanding of IGW properties in microtidal environments, which have been comparatively less studied than meso- and macrotidal coasts in this regard.

XBeach has been subjected to a novel, feasible calibration process against a long time series of field observations of run-up and swash characteristics from a nearby monitoring station, with hindcast data from a basin-scale oceanographic model as wave input. The calibrated model is shown to model swash features with reasonable average skill, although scatter is observed due to congenital discrepancies between the synthetic wave climate and the real swash regime.

A dominance of BLW at the dissipative beach of Sabaudia, especially with intense wave conditions, has been observed. Steady growth of IGW heights is modeled across the shoaling zone for both low and high wave energy conditions, consistently with a global transfer of wave energy toward the lower frequencies from short, swell

waves. Asymmetric IGWs are observed during final shoaling before being finally released in the surf zone; seaward-directed long waves generated at the breakpoint are absent. IGWs stop growing upon entering the surf zone mostly as free waves and are predominantly dissipated by breaking in shallow waters, while friction-based dissipation is considered negligible.

Analysis of frequency-dependent IGW heights as a function of storm intensity shows that the beach experiences a clear transition from a steep-slope regime, with strong amplification and virtually no dissipation of IGW in weak wave climate, to a mild-slope behavior with non-negligible IG dissipation in a 400 m-wide region extending well seaward of the outer bar. Such transition, moreover, occurs at higher β_H than expected. When only the intermediate IG frequencies are considered, however, low tide is able to shift the beach behavior toward a mild-slope regime (reduced R^2) by reducing onshore energy fluxes.

Our study gives the first evidence that the tide is able to exert control over dissipation regimes of a mild sloping beach even in coasts with a small tidal excursion (up to 0.5 m); we thus suggest considering also tidal excursion when analyzing dynamics for which the energy of low-frequency motions is known to be important, for example, sediment mobilization and coastal inundation at gently sloping beaches.

Data Availability Statement

The dataset used for the calibration process and sample wave events simulation in the study is available at the following Zenodo repository referenced in Melito et al. (2021). Version 1.23.5526 of the software XBeach has been used for the calibration process and sample wave events simulation; the model is in the public domain and can be downloaded at the following page: <https://oss.deltares.nl/web/xbeach/>.

Acknowledgments

This study is funded by Circeo National Park and Gargano National Park within the National Biodiversity Strategy promoted by the Ministero dell'Ambiente e della Tutela del Territorio e del Mare (MATTM), Italy (GAB0024444). Financial support from the Office of Naval Research Global (UK) MORSE Project (Research Grant No. N62909-17-1-2148) and the MIUR PRIN 2017 Project, Italy "FUNDamentals of BREAKing wave-induced boundary dynamics – FUNBREAK" (Grant No. 20172B7MY9) is gratefully acknowledged. The authors would like to thank the two anonymous reviewers for their useful comments which improved the quality of the manuscript. Open Access Funding provided by Università Politecnica delle Marche within the CRUI-CARE Agreement.

References

- Aagaard, T., & Holm, J. (1989). Digitization of wave run-up using video records. *Journal of Coastal Research*, 547–551.
- Baldock, T. (2006). Long wave generation by the shoaling and breaking of transient wave groups on a beach. *Proceedings of the Royal Society A: Mathematical, Physical & Engineering Sciences*, 462(2070), 1853–1876. <https://doi.org/10.1098/rspa.2005.1642>
- Baldock, T. (2012). Dissipation of incident forced long waves in the surf zone—Implications for the concept of “bound” wave release at short wave breaking. *Coastal Engineering*, 60(1), 276–285. <https://doi.org/10.1016/j.coastaleng.2011.11.002>
- Baldock, T., & Huntley, D. (2002). Long-wave forcing by the breaking of random gravity waves on a beach. *Proceedings of the Royal Society A: Mathematical, Physical & Engineering Sciences*, 458(2025), 2177–2201. <https://doi.org/10.1098/rspa.2002.0962>
- Baldock, T., Huntley, D., Bird, P., O'Hare, T., & Bullock, G. (2000). Breakpoint generated surf beat induced by bichromatic wave groups. *Coastal Engineering*, 39(2–4), 213–242. [https://doi.org/10.1016/s0378-3839\(99\)00061-7](https://doi.org/10.1016/s0378-3839(99)00061-7)
- Baldock, T., Manoonvoravong, P., & Pham, K. S. (2010). Sediment transport and beach morphodynamics induced by free long waves, bound long waves and wave groups. *Coastal Engineering*, 57(10), 898–916. <https://doi.org/10.1016/j.coastaleng.2010.05.006>
- Battjes, J. A. (1974). Surf similarity. International Conference of Coastal Engineering. In *Coastal engineering proceedings* (Vol. 1, pp. 466–480). <https://doi.org/10.9753/jicce.v14.26>
- Battjes, J. A., Bakkenes, H. J., Janssen, T. T., & vanDongeren, A. R. (2004). Shoaling of subharmonic gravity waves. *Journal of Geophysical Research*, 109(C2), 1–15. <https://doi.org/10.1029/2003JC001863>
- Benson, M. A., & Dalrymple, T. (1967). General field and office procedures for indirect discharge measurements. *Tech. Rep.* <https://doi.org/10.3133/twri03A1>
- Bertin, X., deBakker, A., vanDongeren, A., Coco, G., André, G., Ardhuin, F., & Tissier, M. (2018). Infragravity waves: From driving mechanisms to impacts. *Earth-Science Reviews*, 177, 774–799. <https://doi.org/10.1016/j.earscirev.2018.01.002>
- Bertin, X., Martins, K., Bakker, A., Chataigner, T., Guérin, T., Coulombier, T., & Viron, O. (2020). Energy transfers and reflection of infragravity waves at a dissipative beach under storm waves. *Journal of Geophysical Research: Oceans*, 125(5), e2019JC015714. <https://doi.org/10.1029/2019JC015714>
- Bertin, X., & Olabarrieta, M. (2016). Relevance of infragravity waves in a wave-dominated inlet. *Journal of Geophysical Research: Oceans*, 5418–5435. <https://doi.org/10.1002/2015JC011444>
- Bouguet, J.-Y. (2004). *Camera calibration toolbox for Matlab*. Retrieved from http://www.vision.caltech.edu/bouguetj/calib_doc/index.html
- Collis, W. B., White, P. R., & Hammond, J. K. (1998). Higher-order spectra: The bispectrum and trispectrum. *Mechanical Systems and Signal Processing*, 12(3), 375–394. <https://doi.org/10.1006/mssp.1997.0145>
- Conde-Frias, M., Otero, L., Restrepo, J. C., Ortiz, J. C., Ruiz, J., & Osorio, A. F. (2017). Swash oscillations in a microtidal dissipative beach. *Journal of Coastal Research*, 33(6), 1408–1422. <https://doi.org/10.2112/JCOASTRES-D-16-00147.1>
- Cox, N., Dunkin, L. M., & Irish, J. L. (2013). An empirical model for infragravity swash on barred beaches. *Coastal Engineering*, 81, 44–50. <https://doi.org/10.1016/j.coastaleng.2013.06.008>
- de Bakker, A. T., Brinkkemper, J. A., van der Steen, F., Tissier, M. F., & Ruessink, B. G. (2016). Cross-shore sand transport by infragravity waves as a function of beach steepness. *Journal of Geophysical Research: Earth Surface*, 121(10), 1786–1799. <https://doi.org/10.1002/2016JF003878>
- de Bakker, A. T., Herbers, T. H. C., Smit, P. B., Tissier, M. F. S., & Ruessink, B. G. (2015). Nonlinear infragravity-wave interactions on a gently sloping laboratory beach. *Journal of Physical Oceanography*, 45(2), 589–605. <https://doi.org/10.1175/JPO-D-14-0186.1>
- de Bakker, A. T., Tissier, M. F., & Ruessink, B. G. (2014). Shoreline dissipation of infragravity waves. *Continental Shelf Research*, 72, 73–82. <https://doi.org/10.1016/j.csr.2013.11.013>
- Fiedler, J. W., Brodie, K. L., McNinch, J. E., & Guza, R. T. (2015). Observations of runup and energy flux on a low-slope beach with high-energy, long-period ocean swell. *Geophysical Research Letters*, 42(22), 9933–9941. <https://doi.org/10.1002/2015GL066124>

- Goda, Y. (2000). *Random Seas and Design of Maritime Structures* (Vol. 15). World Scientific. <https://doi.org/10.1142/3587>
- Guza, R. T., & Thornton, E. B. (1982). Swash oscillations on a natural beach. *Journal of Geophysical Research*, 87(C1), 483–491. <https://doi.org/10.1029/jc087ic01p00483>
- Guza, R. T., Thornton, E. B., & Holman, R. A. (1984). Swash on steep and shallow beaches. *Coastal Engineering Proceedings*, 1(19), 48. <https://doi.org/10.9753/icce.v19.48>
- Hartley, R., & Zisserman, A. (2004). *Multiple view Geometry in computer vision*. Cambridge University Press. <https://doi.org/10.1017/CBO9780511811685>
- Hasselmann, K., Munk, W., & MacDonald, G. (1962). Bispectra of ocean waves. In *Proceedings of the symposium on time series analysis* (pp. 125–139).
- Herbers, T. H. C., Elgar, S., & Guza, R. T. (1995). Generation and propagation of infragravity waves. *Journal of Geophysical Research*, 100(C12), 24863–24872. <https://doi.org/10.1029/95jc02680>
- Holland, K. T., Holman, R. A., Lippmann, T. C., Stanley, J., & Plant, N. (1997). Practical use of video imagery in nearshore oceanographic field studies. *IEEE Journal of Oceanic Engineering*, 22(1), 81–92. <https://doi.org/10.1109/48.557542>
- Holman, R. A., Sallenger, A. H., Lippmann, T. C., & Haines, J. W. (1993). The application of video image processing to the study of nearshore processes. *Oceanography*, 6(3), 78–85. <https://doi.org/10.5670/oceanog.1993.02>
- Hughes, M. G., Aagaard, T., Baldock, T. E., & Power, H. E. (2014). Spectral signatures for swash on reflective, intermediate and dissipative beaches. *Marine Geology*, 355, 88–97. <https://doi.org/10.1016/j.margeo.2014.05.015>
- Inch, K., Davidson, M., Masselink, G., & Russell, P. (2017). Observations of nearshore infragravity wave dynamics under high energy swell and wind-wave conditions. *Continental Shelf Research*, 138, 19–31. <https://doi.org/10.1016/j.csr.2017.02.010>
- Korres, G., Ravdas, M., & Zacharioudaki, A. (2019). *Mediterranean Sea waves hindcast (CMEMS_MED_WAVES)*. Copernicus Monitoring Environment Marine Service (CMEMS). https://doi.org/10.25423/CMCC/MEDSEA_HINDCAST_WAV_006_012
- Lippmann, T. C., & Holman, R. A. (1989). Quantification of sand bar morphology: A video technique based on wave dissipation. *Journal of Geophysical Research*, 94(C1), 995–1011. <https://doi.org/10.1029/JC094C01p00995>
- Longuet-Higgins, M. S., & Stewart, R. W. (1964). Radiation stresses in water waves; a physical discussion, with applications. *Deep Sea Research and Oceanographic Abstracts*, 11(4), 529–562. [https://doi.org/10.1016/0011-7471\(64\)90001-4](https://doi.org/10.1016/0011-7471(64)90001-4)
- Matheen, N., Harley, M. D., Turner, I. L., Splinter, K. D., Simmons, J. A., & Thran, M. C. (2021). Bathymetric data requirements for operational coastal erosion forecasting using XBeach. *Journal of Marine Science and Engineering*, 9(10), 1053. <https://doi.org/10.3390/jmse9101053>
- McCall, R. T., Van Thiel de Vries, J. S. M., Plant, N. G., Van Dongeren, A. R., Roelvink, J. A., Thompson, D. M., & Reniers, A. J. H. M. (2010). Two-dimensional time dependent hurricane overwash and erosion modeling at Santa Rosa Island. *Coastal Engineering*, 57(7), 668–683. <https://doi.org/10.1016/j.coastaleng.2010.02.006>
- Melito, L., Parlagreco, L., Devoti, S., & Brocchini, M. (2021). Dataset for XBeach model calibration and simulation of sample storms in an intermediate-to-dissipative, microtidal coast (Sabaudia, Italy). [Dataset]. <https://doi.org/10.5281/zenodo.5470253>
- Melito, L., Parlagreco, L., Perugini, E., Postacchini, M., Devoti, S., & Brocchini, M. (2020). Sandbar dynamics in microtidal environments: Migration patterns in unprotected and bounded beaches. *Coastal Engineering*, 161, 103768. <https://doi.org/10.1016/j.coastaleng.2020.103768>
- Moura, T., & Baldock, T. (2017). Remote sensing of the correlation between breakpoint oscillations and infragravity waves in the surf and swash zone. *Journal of Geophysical Research: Oceans*, 122(4), 3106–3122. <https://doi.org/10.1002/2016JC012233>
- Moura, T., & Baldock, T. E. (2018). New evidence of breakpoint forced long waves: Laboratory, numerical, and field observations. *Journal of Geophysical Research: Oceans*, 123(4), 2716–2730. <https://doi.org/10.1002/2017JC013621>
- Oh, J.-E., Jeong, W.-M., Chang, Y. S., & Oh, S.-H. (2020). On the separation period discriminating gravity and infragravity waves off Gyeongpo Beach, Korea. *Journal of Marine Science and Engineering*, 8(3), 167. <https://doi.org/10.3390/jmse8030167>
- Okiihiro, M., & Guza, R. (1995). Infragravity energy modulation by tides. *Journal of Geophysical Research*, 100(C8), 16143–16148. <https://doi.org/10.1029/95jc01545>
- Okiihiro, M., Guza, R., & Seymour, R. (1993). Excitation of seiche observed in a small harbor. *Journal of Geophysical Research*, 98(C10), 18201–18211. <https://doi.org/10.1029/93jc01760>
- Otsu, N. (1979). A threshold selection method from gray-level histograms. *IEEE Transactions on Systems, Man, and Cybernetics*, 9(1), 62–66. <https://doi.org/10.1109/tsmc.1979.4310076>
- Parlagreco, L., Melito, L., Devoti, S., Perugini, E., Soldini, L., Zitti, G., & Brocchini, M. (2019). Monitoring for coastal resilience: Preliminary data from five Italian sandy beaches. *Sensors*, 19(8), 1854. <https://doi.org/10.3390/s19081854>
- Pinault, J., Morichon, D., & Roeber, V. (2020). Estimation of irregular wave runup on intermediate and reflective beaches using a phase-resolving numerical model. *Journal of Marine Science and Engineering*, 8(12), 993. <https://doi.org/10.3390/jmse8120993>
- Pomeroy, A., Lowe, R., Symonds, G., VanDongeren, A., & Moore, C. (2012). The dynamics of infragravity wave transformation over a fringing reef. *Journal of Geophysical Research*, 117(C11), C11022. <https://doi.org/10.1029/2012JC008310>
- Roelvink, D., Reniers, A., van Dongeren, A., van Thiel de Vries, J., McCall, R., & Lescinski, J. (2009). Modelling storm impacts on beaches, dunes and barrier islands. *Coastal Engineering*, 56(11–12), 1133–1152. <https://doi.org/10.1016/j.coastaleng.2009.08.006>
- Ruessink, B. G. (1998a). Bound and free infragravity waves in the nearshore zone under breaking and nonbreaking conditions. *Journal of Geophysical Research*, 103(C6), 12795–12805. <https://doi.org/10.1029/98JC00893>
- Ruessink, B. G. (1998b). The temporal and spatial variability of infragravity energy in a barred nearshore zone. *Continental Shelf Research*, 18(6), 585–605. [https://doi.org/10.1016/S0278-4343\(97\)00055-1](https://doi.org/10.1016/S0278-4343(97)00055-1)
- Ruessink, B. G., Kleinhans, M. G., & van den Beukel, P. G. L. (1998). Observations of swash under highly dissipative conditions. *Journal of Geophysical Research*, 103(C2), 3111–3118. <https://doi.org/10.1029/97jc02791>
- Ruffini, G., Briganti, R., Alsinà, J. M., Brocchini, M., Dodd, N., & McCall, R. (2020). Numerical modeling of flow and bed evolution of bichromatic wave groups on an intermediate beach using nonhydrostatic XBeach. *Journal of Waterway, Port, Coastal, and Ocean Engineering*, 146(1), 04019034. [https://doi.org/10.1061/\(asce\)ww.1943-5460.0000530](https://doi.org/10.1061/(asce)ww.1943-5460.0000530)
- Ruggiero, P., Komar, P. D., McDougal, W. G., Marra, J. J., & Beach, R. A. (2001). Wave runup, extreme water levels and the erosion of properties backing beaches. *Journal of Coastal Research*, 17(2), 407–419.
- Rutten, J., Freyermuth, A. T., & Puleo, J. (2021). Uncertainty in runup predictions on natural beaches using XBeach nonhydrostatic. *Coastal Engineering*, 17, 103869. <https://doi.org/10.1016/j.coastaleng.2021.103869>
- Senechal, N., Coco, G., Bryan, K. R., & Holman, R. A. (2011). Wave runup during extreme storm conditions. *Journal of Geophysical Research*, 116(7), C07032. <https://doi.org/10.1029/2010JC006819>
- Sheremet, A., Guza, R. T., Elgar, S., & Herbers, T. H. (2002). Observations of nearshore infragravity waves: Seaward and shoreward propagating components. *Journal of Geophysical Research*, 107(8), 3095. <https://doi.org/10.1029/2001jc000970>

- Soldini, L., Antuono, M., & Brocchini, M. (2013). Numerical modeling of the influence of the beach profile on wave run-up. *Journal of Waterway, Port, Coastal, and Ocean Engineering*, 139(1), 61–71. [https://doi.org/10.1061/\(asce\)ww.1943-5460.0000163](https://doi.org/10.1061/(asce)ww.1943-5460.0000163)
- Soulsby, R. (1997). *Dynamics of marine sands*. Thomas Telford Publishing. <https://doi.org/10.1680/doms.25844>
- Stockdon, H. F., Holman, R. A., Howd, P. A., & Sallenger, A. H. (2006). Empirical parameterization of setup, swash, and runup. *Coastal Engineering*, 53(7), 573–588. <https://doi.org/10.1016/j.coastaleng.2005.12.005>
- Stockdon, H. F., Thompson, D. M., Plant, N. G., & Long, J. W. (2014). Evaluation of wave runup predictions from numerical and parametric models. *Coastal Engineering*, 92, 1–11. <https://doi.org/10.1016/j.coastaleng.2014.06.004>
- Symonds, G., Huntley, D. A., & Bowen, A. J. (1982). Two-dimensional surf beat: Long wave generation by a time-varying breakpoint. *Journal of Geophysical Research*, 87(C1), 492–498. <https://doi.org/10.1029/jc087ic01p00492>
- Taramelli, A., Cappucci, S., Valentini, E., Rossi, L., & Lisi, I. (2020). Nearshore sandbar classification of Sabaudia (Italy) with LiDAR data: The FHyl approach. *Remote Sensing*, 12(7), 1053. <https://doi.org/10.3390/rs12071053>
- Thomson, J., Elgar, S., Raubenheimer, B., Herbers, T. H., & Guza, R. T. (2006). Tidal modulation of infragravity waves via nonlinear energy losses in the surfzone. *Geophysical Research Letters*, 33(5), L05601. <https://doi.org/10.1029/2005GL025514>
- Valentini, N., Saponieri, A., Danisi, A., Pratola, L., & Damiani, L. (2019). Exploiting remote imagery in an embayed sandy beach for the validation of a runup model framework. *Estuarine, Coastal and Shelf Science*, 225, 106244. <https://doi.org/10.1016/j.ecss.2019.106244>
- van Dongeren, A., Battjes, J., Janssen, T., vanNoorloos, J., Steenhauer, K., Steenbergen, G., & Reniers, A. (2007). Shoaling and shoreline dissipation of low-frequency waves. *Journal of Geophysical Research*(2), C02011. <https://doi.org/10.1029/2006JC003701>
- Van Gent, M., & Giarrusso, C. (2005). Influence of foreshore mobility on wave boundary conditions. In *Proceedings of the Fifth International Conference on ocean waves Measurement and analysis*.
- Vousdoukas, M. I., Wziatek, D., & Almeida, L. P. (2012). Coastal vulnerability assessment based on video wave run-up observations at a mesotidal, steep-sloped beach. *Ocean Dynamics*, 62(1), 123–137. <https://doi.org/10.1007/s10236-011-0480-x>
- Website of the Italian Tide Gauge Network. (2021). Retrieved from <https://www.mareografico.it>
- Williams, M. E., & Stacey, M. T. (2016). Tidally discontinuous ocean forcing in bar-built estuaries: The interaction of tides, infragravity motions, and frictional control. *Journal of Geophysical Research: Oceans*, 121(1), 571–585. <https://doi.org/10.1002/2015JC011166>
- Willmott, C. J., Robeson, S. M., & Matsuura, K. (2012). A refined index of model performance. *International Journal of Climatology*, 32(13), 2088–2094. <https://doi.org/10.1002/joc.2419>
- Wright, L. D., & Short, A. D. (1984). Morphodynamic variability of surf zones and beaches: A synthesis. *Marine Geology*, 56(1–4), 93–118. [https://doi.org/10.1016/0025-3227\(84\)90008-2](https://doi.org/10.1016/0025-3227(84)90008-2)